Nanostructured Architectures for Colloidal Quantum Dot Solar Cells

by

Joel Jean

B.S., Electrical Engineering, Stanford University, 2011

Submitted to the Department of Electrical Engineering and Computer Science
in partial fulfillment of the requirements for the degree of

Master of Science
in Electrical Engineering
at the Massachusetts Institute of Technology

June 2013

Signature of Author: _____

Joel Jean
Department of Electrical Engineering and Computer Science
May 22, 2013

Certified by: _____

Vladimir Bulović
Professor of Electrical Engineering and Computer Science
Thesis Supervisor

Accepted by: _____

Leslie A. Kolodziejski
Professor of Electrical Engineering and Computer Science
Chair, Committee for Graduate Students

Nanostructured Architectures for Colloidal Quantum Dot Solar Cells

by Joel Jean

Submitted to the Department of Electrical Engineering and Computer Science
in partial fulfillment of the requirements for the degree of
Master of Science

Abstract

This thesis introduces a novel ordered bulk heterojunction architecture for colloidal quantum dot (QD) solar cells. Quantum dots are solution-processed nanocrystals whose tunable bandgap energies make them a promising active-layer candidate for next-generation optoelectronic devices, including solar cells and light-emitting diodes. Despite rapid advances in performance, however, modern QD solar cells remain limited by a fundamental trade-off between light absorption and photocarrier collection due to poor electronic transport. Vertically aligned arrays of ZnO nanowires can decouple absorption and collection: The nanowires penetrate into the QD film and serve as highly-conductive channels for extracting photogenerated electrons from deep within the film. After optimizing the nanowire growth and device fabrication processes, we find that incorporating nanowires boosts the photocurrent and the efficiency of planar QD photovoltaic devices by 50% and 35%, respectively. The demonstrated AM1.5G power conversion efficiency of 4.9% is among the highest ever reported for a ZnO-based QD solar cell. We further show that graphene can serve as a viable alternative to tin-doped indium oxide (ITO) as a transparent conductive electrode for thin-film optoelectronics. We grow ZnO nanowires on graphene and fabricate prototype graphene-based ordered bulk heterojunction QD devices with photovoltaic performance approaching that of ITO-based solar cells.

Our work shows that nanostructured architectures can substantially improve QD solar cell performance, and that a simple, low-temperature, bottom-up solution growth process can produce nanowire alignment and device performance matching that of top-down synthetic processes, with the added advantage of compatibility with a variety of rigid and flexible substrates. The 1-D nanostructure design principles we propose and apply here can be generalized to a broad range of optoelectronic device applications. This study of scalable bottom-up processing of ZnO nanowire-based QD solar cells suggests that 1-D nanostructures may be the key to enhancing the efficiency and hence the economic viability of quantum dot photovoltaics.

Thesis Supervisor: Vladimir Bulović
Title: Professor of Electrical Engineering

Acknowledgments

THIS thesis is dedicated to my family—Mom, Dad, and Neal—whose love and support will never flag or fail.

I want to thank my advisor Vladimir Bulović, whose good cheer and charisma, passion and compassion, together make him the most inspiring scientific communicator and leader I know. His booming laughter echoes through the hallways of Building 13 and draws out the best in all of us.

But Vladimir's strongest trait—what has most influenced my life at MIT—is his ability to find good people, to fill and replenish his group with wonderful students and post-docs who come together inside and outside the lab to make the world a better place. From undergrads to grad students to post-docs to alumni, ONE Lab makes grad school a team sport, one that I hope to keep playing for at least a few more years. I am deeply indebted to all past and current group members for establishing the lab, shaping its culture, and setting the bar for research achievement unreasonably high.

In particular, I want to thank Patrick Brown for being a true friend and consummate scientist. He laid the foundation for my work on quantum dot solar cells, and every experimental result in this thesis bears a trace of his influence. Patrick lends logical clarity to any debate that doesn't involve Notre Dame football, and he cares more than anyone about humanity's collective future.

Tim Osedach and Trisha Andrew have shaped my MIT experience with their friendship and advice. Tim is a kindred spirit, a far-sighted futurist—I would never miss a chance to engage in one of his extreme thought experiments. At first intimidating and ultimately irreplaceable, Trisha remains an intensely loyal friend and an über-dedicated scientist. Her uncensored spirit and unchecked laughter kept me entertained in lab, even at 3AM.

I thank the ONE Lab PV team—Andrea Maurano, Dong Kyun Ko, Jill Macko, and Patrick—for their constant support and wisdom, and Apoorva Murarka for tolerating my office antics. My 2011 classmates—Farnaz Niroui, Katherine Song, Eletha Flores, Wendi Chang, and Mandy Woo—deserve personal mention for indulging me with unwavering commiseration, collaboration, and companionship. Geoffrey Supran shares my deep-seated interest in the world's energy destiny, and our conversations keep me grounded in the big-picture questions of scientific research. Annie Wang, Gleb Akselrod, Yasu

Shirasaki, Ronny Costi, Parag Deotare, Tom Mahony, Christina Hanson, and Su Kyung Suh have variously served as collaborator, critic, mentor, consultant, teacher, sister, psychologist, and friend; they have enriched these early years of graduate school by their very presence. I also want to thank Monica Pegis, the real boss of ONE Lab, for sweeping away the obstacles in my research life and for keeping Vladimir on his game.

I would be remiss not to acknowledge fellow travelers in this ongoing journey. I thank Silvija Gradečak and her group, my primary collaborators in this work. Sehoon Chang provided the ZnO nanowire samples that kicked off this entire enterprise; his cheerful optimism and expertise in nanowire growth and characterization has kept our collaboration both fun and productive. Hyesung Park, Jayce Cheng, and Paul Rekemeyer also deserve special mention; Hyesung led the work on graphene devices, and all three contributed significant time, effort, and insight to the results in this thesis. The $\sim 10^{19}$ quantum dots used in this work were born of the expertise of Moungi Bawendi and his group—in particular I would like to thank Darcy Wanger and Jenn Scherer for their friendship and boundless passion for quantum dots.

I want to thank my former research mentors, Igor Bargatin and Roger Howe. Both taught me semiconductor device physics during my sophomore year at Stanford—Igor introduced me to nanowires that summer—and I haven't looked back since.

I owe one final acknowledgment to my extended family around the world, my longtime friends in Ohio and at Stanford, and most of all, to my friends Carrie, Stephen, Danica, Kendall, William, Erin, Yi, Lily, Kelli, Aaron, Joel, and Alex, with whom I embarked on this MIT adventure. Some might call it a scavenger hunt—and it's not over yet.

Contents

List of Figures

Chapter 1

Introduction

EVERY human being on Earth lives within sight of an energy source that has fuel enough to burn for five billion years. But in the eight minutes and 150 million kilometers before solar radiation enters Earth's atmosphere, the inverse-square law absconds with the vast majority of the sun's blackbody output, and we humans are left to squabble over mere energetic residue with the other passengers of our singular spaceship. These meager leftovers have sustained—nay, they have nourished—the past and present of humanity and of all life on this planet. All who would pass on a world unmarred to future generations would do well to remember the power of starlight. But the sun is just one side of the equation: To make sustainable energy from outer space a reality, we need an appropriate collector for converting solar photons into useful electrons. And given the energetically diffuse nature of sunlight, we must cover large swaths of the Earth's surface with such collectors to satiate the terawatt-scale appetite of modern civilization.

Enter quantum dots (QDs). Colloidal quantum dots are solution-born nanocrystals that can be tuned by quantum confinement to absorb and emit light efficiently at a wide range of wavelengths (e.g., to match the solar spectrum). Lead sulfide (PbS) QDs are particularly well suited for solar energy conversion, with an absorption edge tunable from the near-infrared through the visible and stability in ambient atmosphere. Solar cells based on colloidal PbS QDs could thus provide an inexpensive, flexible alternative to conventional silicon and thin-film photovoltaics (PVs). Solid-state quantum dot photovoltaic (QDPV) devices constitute the most recent addition to the NREL photovoltaic efficiency charts (Figure 1.4). Despite their theoretical benefits and upward trajectory, however, the question remains whether QDPVs can achieve the efficiencies required to offset the fixed costs of a complete photovoltaic system, including structural and electrical components, labor, and installation[1]. Therein lies the opportunity.

This thesis addresses one of the primary limitations on modern QDPV performance:

inefficient charge carrier extraction. Poor electron transport in QD films restricts the thickness of current QDPV devices to far below the thickness required for full light absorption. To decouple absorption from carrier collection, we introduce a nanostructured device architecture—the ordered bulk heterojunction—and demonstrate a significant relative improvement in the photocurrent and the power conversion efficiency of colloidal QD solar cells[2].

The rest of Chapter 1 establishes the key concepts and motivations for solar energy generation using colloidal quantum dots. We briefly review the solar resource and the key approaches to solar energy conversion, then introduce a promising third-generation PV technology: colloidal quantum dot solar cells. We discuss contemporary QD solar cell architectures and the primary challenges facing QDPVs today. Chapter 2 introduces the ordered bulk heterojunction architecture and describes the growth and optimization of zinc oxide (ZnO) nanowires and the subsequent fabrication of nanowire-based QD photovoltaic (NW-QDPV) devices. Chapter 3 demonstrates the performance of NW-QDPVs and presents some basic guidelines for the design of nanostructured solar cells, based on investigations of the effect of morphology and structure on nanostructured QDPVs. Chapter 4 explores the use of graphene as a transparent, indium-free electrode material for thin-film solar cells, with a proof-of-concept demonstration of nanowire-based QDPVs fabricated on a graphene cathode. Chapter 5 presents a vision for the future of QDPV development and outlines a path forward for QDPV research efforts. Chapter 6 summarizes and concludes the thesis.

■ 1.1 The Solar Resource

Solar radiation is the most abundant of Earth's renewable energy resources—the solar energy flux incident on the planetary sphere ($\sim 1\times10^{17}$ W) is four orders of magnitude higher than the current global energy demand ($\sim 1\times10^{13}$ W)—and many other renewable energy sources also originate from solar radiation. The sun can be closely approximated by a black body at a temperature of $T_{sun} = 5780$ K emitting isotropically from a distance of $\sim 1.5\times10^{8}$ km from Earth. Unavoidable inverse-square attenuation losses result in a power density (the "solar constant") of 1353 W m^{-2} outside Earth's atmosphere (AM0). Further atmospheric absorption in the UV (by O_2, O_3, and N_2) and in the near-infrared (by O_2, CO_2, and water vapor) yields an average irradiance of 1000 W m^{-2} = 100 mW cm^{-2} at the Earth's surface (AM1.5G).[1] The solar irradiance and photon

[1] Solar cell testing standards typically denote solar irradiance spectra based on the relative atmospheric depth—the air mass (AM)—through which radiation must travel before reaching the Earth's surface.

flux spectra are shown in Figure 1.1. A simple back-of-the-envelope calculation[2] suggests that covering around 1% of Earth's land area with 10% efficient solar converters would satisfy global energy demand.

Yet in spite of the overwhelming scale of raw solar energy resources, solar harvesting accounted for just 0.1% of global electricity production in 2012[3]. Only in the past decade has the economic and political environment become favorable for solar energy production on a global scale, with an alignment of government subsidies and rising unease about the environmental impact of fossil fuels providing relative market stability and an impetus for substantial investment in research and development efforts on solar technologies.

■ 1.2 Solar Energy Generation

Solar energy can be converted into useful work in three energetic end forms: thermal, chemical, and electrical energy. Solar-to-thermal applications use solar radiation to heat water or another absorbing medium directly and efficiently—e.g., for heating or cooking. Solar-to-chemical approaches store radiation energy in conventional fuels—e.g., liquid hydrocarbons, hydrogen, syngas—hence offering a solution to the oft-cited intermittency problem associated with most renewable energy technologies. We focus here on the third option, solar-to-electric energy conversion.

To convert radiation into low-entropy electrical energy, we can take one of two primary approaches: solar thermal[3] or solar photovoltaic energy conversion. Solar thermal converters use concentrated solar radiation to heat water or another thermal transfer medium (e.g., molten salt) and drive a standard thermodynamic cycle for electricity production. But while solar thermal systems can reach relatively high power conversion efficiencies, the concentrating optics and high temperatures required for

AM0 corresponds to the irradiance spectrum outside the Earth's atmosphere and is used to characterize solar cells for space applications. AM1 and AM1.5 correspond to the spectrum at sea level with the sun directly overhead and at a global "spatiotemporal average" solar zenith angle of $cos^{-1}(\frac{1}{1.5}) = 48.2°$, respectively. An additional G label (i.e., AM1.5G) denotes "global," hence including both direct and diffuse (scattered) radiation.

[2]Assume 100 W m^{-2} time-averaged insolation (equivalent to 2.4 kWh m^{-2} day^{-1}, a conservative estimate) and 10% power conversion efficiency. The estimated land area needed to satisfy a global power demand of 10 TW is then $1{\times}10^{13}$ W $\times \frac{1\ m^2}{10\%\times(1{\times}10^2\ W)} \times \frac{1\ km^2}{1{\times}10^6\ m^2} = 1{\times}10^6\ km^2$, corresponding to a fractional coverage of Earth's total land area of $\frac{1{\times}10^6\ km^2}{0.3\times(5{\times}10^8\ km^2)} = 0.67\%$.

[3]Note that solar thermal electricity generation is not to be confused with solar-to-thermal energy conversion, where the energetic endpoint is heat, not electricity. The former process could perhaps be more accurately (and more unwieldily) dubbed solar-thermal-electric conversion.

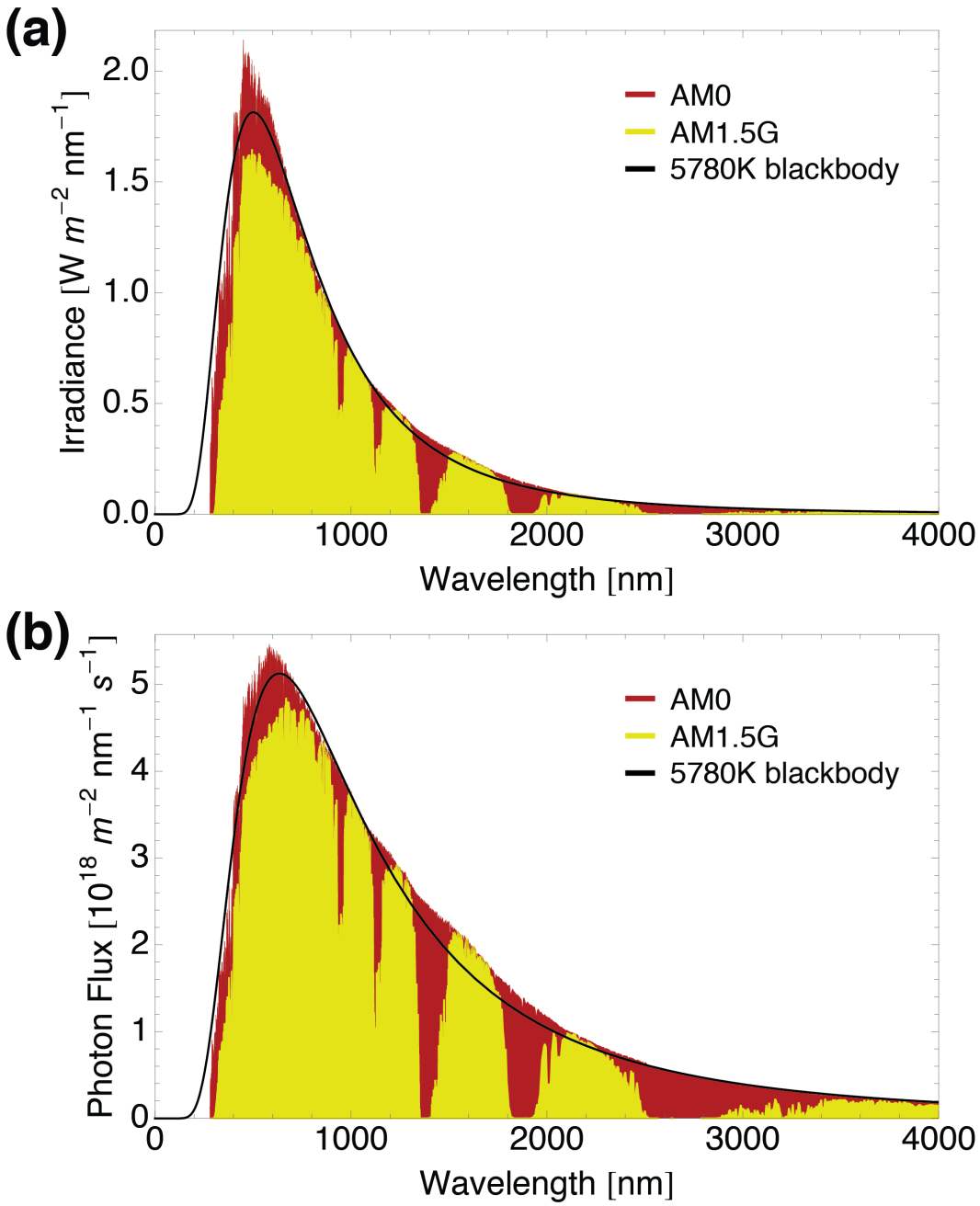

Figure 1.1: *The solar spectrum. (a) Solar irradiance and (b) photon flux spectra corresponding to AM0 (red), AM1.5G (yellow), and 5780 K blackbody (black). Note that the key quantity for conventional solar photovoltaics is the spectral photon flux, as each absorbed photon yields the same energy output after thermalization—a fraction of the band gap energy* E_g.

efficient operation limit their utility for distributed energy generation—for example, in grid-isolated or residential deployments—thus sacrificing one of the primary advantages of the ubiquitous solar energy resource. The most promising method for utility-scale and distributed solar electricity generation thus remains solar photovoltaics, which uses an energetically asymmetric semiconductor device (the "solar cell") to absorb light, separate electric charge carriers (i.e., electrons and holes), and produce electrical power.

■ 1.3 Basics of Solar Photovoltaics

The operation of a solar cell is best understood with the aid of an energy band diagram (Figure 1.2)—band diagrams are used extensively throughout this work to illustrate the effect of physical and chemical modifications on device operation. Incident photons are absorbed in either the depletion region or one of the quasi-neutral regions, generating an exciton or electron-hole pair. Electrons and holes relax to the band edge, split up due to the electric field in the depletion region, and accumulate in the n-type and p-type quasi-neutral regions, respectively. The resulting separation of the quasi-Fermi levels E_{Fn} and E_{Fp} gives rise to an output photovoltage $V_{out} = E_{Fn} - E_{Fp}$, and the flow of carriers out of the respective contacts yields a photocurrent J_{out}.

Basic electrical characterization reveals the photovoltaic performance of a solar cell, with current density-voltage (J-V) characteristics as the output. An equivalent circuit and example J-V curve for a solar cell in the dark and under illumination is shown in Figure 1.3. Six primary photovoltaic figures of merit are indicated on the plot; the product of the short-circuit current density (J_{SC}), open-circuit voltage (V_{OC}), and fill factor (FF) is divided by the incident optical power to calculate the power conversion efficiency $PCE = \frac{J_{SC} \times V_{OC} \times FF}{P_{in}}$. To maximize efficiency, we want to maximize J_{SC}, V_{OC}, and FF, the last of which requires minimizing the series resistance R_s and maximizing the shunt resistance R_{sh}.

No discussion of solar photovoltaics is complete without an appearance of the oft-revised world-record solar cell power conversion efficiency chart, compiled by the National Renewable Energy Laboratory (NREL) and shown in Figure 1.4. We focus here on the bottom-right corner of the chart, where nanomaterial-based PVs have recently emerged as a promising and rapidly improving family of solar cells with unprecedented cost, scaling, and flexibility advantages over conventional bulk and thin-film devices. In this category lies the focus of this work: colloidal quantum dot solar cells.

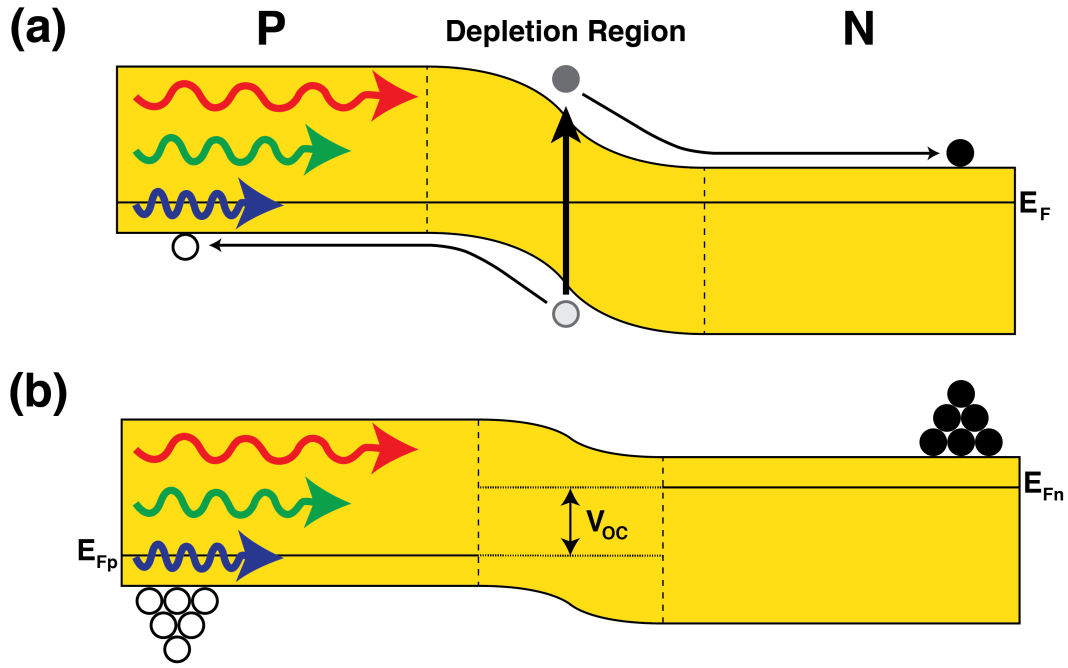

Figure 1.2: *Model energy band diagram for a homojunction solar cell under illumination at (a) short-circuit and (b) open-circuit. Absorption of a photon generates an electron-hole pair, which is subsequently separated into free carriers by the electric field in the depletion region. Dashed lines indicate the edges of the depletion region, which shrinks under forward bias. Accumulation of electrons on the n-side of the junction and holes on the p-side splits the quasi-Fermi levels (E_{Fn} and E_{Fp}, respectively) and generates a potential difference corresponding to the solar cell open-circuit voltage V_{OC}.*

■ 1.4 Colloidal Quantum Dots

Colloidal quantum dots (QDs) are solution-processed nanocrystals with diameters of 1-10 nm.[4] Common semiconducting QD materials include lead and cadmium chalcogenides (e.g., PbS, PbSe, CdS, CdSe). While QDs exhibit several unique physical phenomena, the primary characteristic of interest for photovoltaics and other optoelectronic applications is their tunable band gap: The quantum size effect—spatial confinement beyond the exciton Bohr radius—allows continuous tuning of the fundamental band gap, and hence the onset of optical absorption, from the bulk value up to significantly higher energies, simply by changing the QD size. By starting with a semi-

[4]The term"quantum dot" is often used to refer to any quasi zero-dimensional (0-D) system—i.e., a system exhibiting quantum confinement in all three spatial dimensions. Such systems can be formed by a variety of methods, including vapor- or solution-phase self-assembly and colloidal synthesis. In particular, we differentiate between epitaxial and colloidal quantum dots and focus here on the latter.

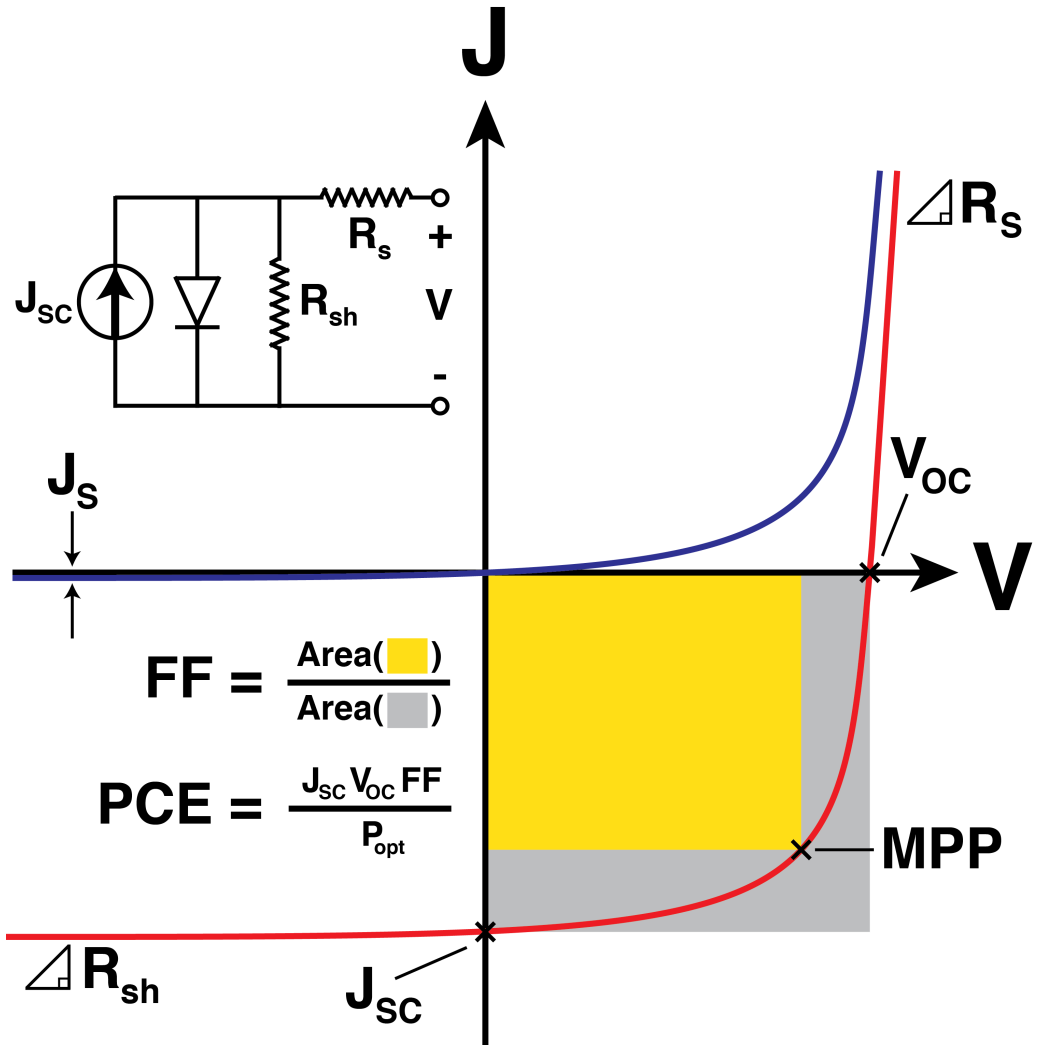

Figure 1.3: *Model current density-voltage (J-V) characteristics for a solar cell in the dark (blue) and under illumination (red). The primary photovoltaic performance parameters are identified on the graph: short-circuit current density (J_{SC}), open-circuit voltage (V_{OC}), fill factor (FF), power conversion efficiency (PCE), series resistance (R_s), and shunt resistance (R_{sh}). Inset: Equivalent circuit for a solar cell.*

conductor with an infrared bulk band gap (e.g., PbS, $E_g = 0.41$ eV), we can tune the absorption edge from the near-infrared through the visible, spanning the range relevant for solar energy conversion (Figure 1.5). This wide absorption tunability permits us modest control over the valence and conduction band edge energies and hence over charge transfer across heterointerfaces. Furthermore, using QDs as the primary photoactive

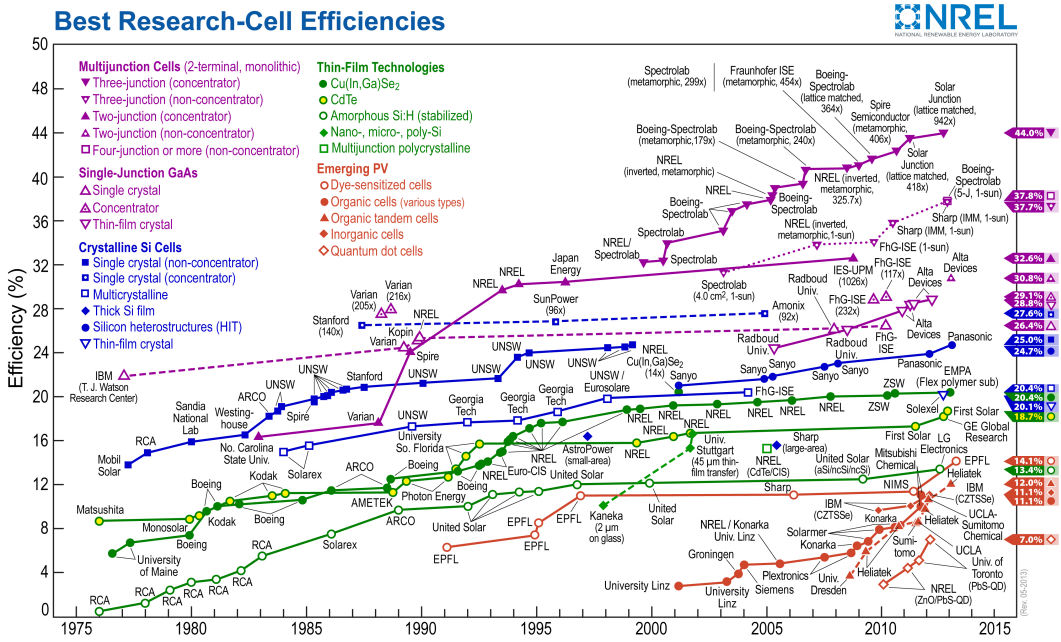

Figure 1.4: *Solar power conversion efficiency records for major classes of solar cells (revised May 2013). Courtesy of NREL.*

layer enables IR-sensitive multijunction solar cells in a single material system[4, 5].

Colloidal QDs are synthesized by a hot-injection process in which precursors, organic surfactants, and solvents are heated until the precursors dissociate and form active atomic or molecular species. With proper control of monomer concentrations, subsequent nucleation and growth yields colloidal nanocrystals with a monodisperse size distribution[6, 7]. The organic surfactants, or ligands, prevent uncontrolled aggregation during growth and allow the QDs to be dispersed in various solvents. Following synthesis, QDs are often cleaned by precipitation with orthogonal solvents to remove excess precursors and surfactants and tighten the size distribution[7], then redispersed to allow long-term storage and facilitate formation of smooth QD films on various surfaces.

Colloidal QDs can be deposited to form thin films by a variety of solution deposition techniques, including spin-casting, dip-coating, spray-painting, ink-jet printing, or contact printing. Sequential layer-by-layer spin-casting is the most widely used technique for QD optoelectronics and yields dense, semiconducting QD films with thicknesses of tens to hundreds of nanometers. Electronic transport through such films typically occurs by a combination of thermally-activated hopping and tunneling between nearby QDs, and

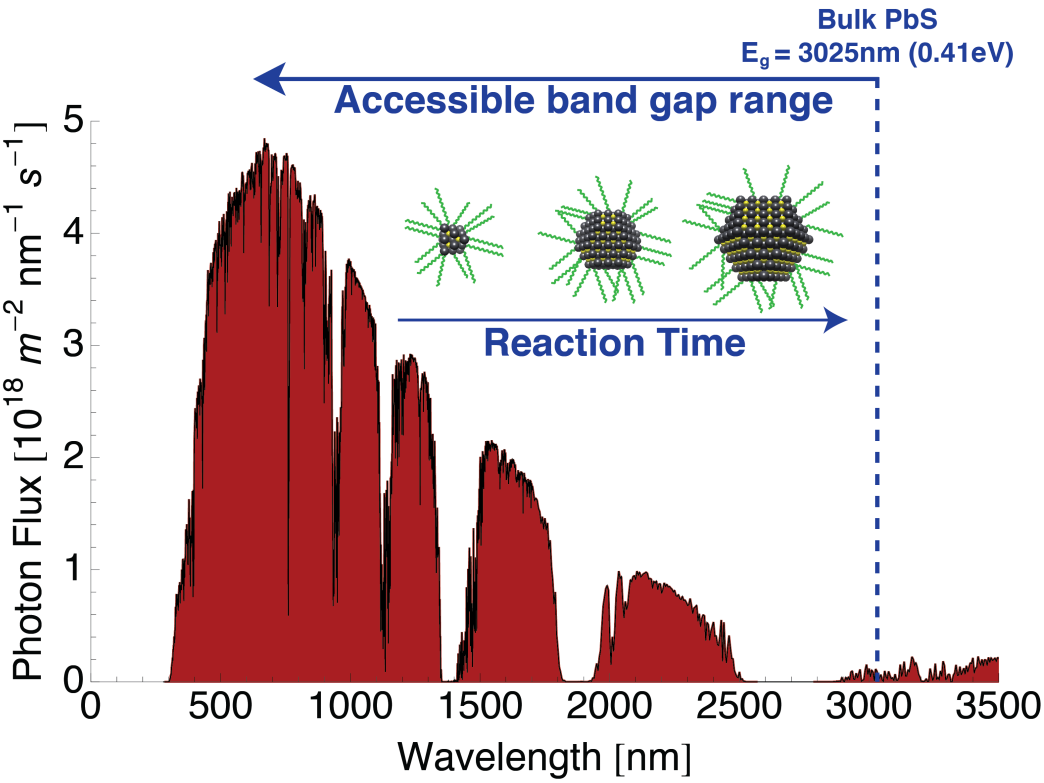

Figure 1.5: *Accessible band gap range using PbS quantum dots. The band gap (first exciton absorption peak) of PbS QDs can be tuned from the near-infrared through the visible to match the AM1.5G solar spectrum.*

hence can be optimized by adjusting tunnel barrier characteristics—e.g., by modifying the organic capping ligands[8]. Although colloidal QD films lack long-range order and exhibit strong localization of electronic wavefunctions, their high effective dielectric constant (e.g., ∼15-20 for PbS[8]) and low exciton binding energies may allow photogenerated excitons to dissociate even in the absence of an electric field. The resulting dominance of free carrier transport, along with the presence of localized dopant-like states, allows most QD device operating characteristics to be interpreted accurately and intuitively using band diagrams, with band-bending similar to that found in conventional inorganic semiconductor devices. Such correspondences have catalyzed the use of QD films as the photoactive layer in photovoltaic devices.

■ 1.5 Quantum Dot Solar Cells

Solar cells employing colloidal quantum dots have in recent years emerged as a promising third-generation photovoltaic technology. Quantum dot solar cells share many of the advantages of organic photovoltaics (OPVs), including low-temperature solution processing[8], environmentally-abundant active materials[9], and compatibility with inexpensive and flexible substrates[10]. Although they remain less efficient than OPVs, solid-state QDPVs have advanced faster, with AM1.5G power conversion efficiencies climbing from 1.8% in 2008[11] to over 7% in 2012[12] (Figure 1.4). A recent theoretical analysis of nanostructured thin-film photovoltaics has suggested that single-junction QDPV efficiencies of up to 15% may be practically achievable[13].

Lead chalcogenide nanocrystals in particular could enhance the performance and practicality of QDPV devices, enabling bandgap tunability from the near infrared through the visible[14] and, with PbS QDs, stability in ambient atmosphere[15, 16, 17]. Most recent high-performing QDPVs have paired PbS QDs with a wide-bandgap metal oxide window layer (i.e., ZnO or TiO_2) in an inverted *np*-heterojunction architecture[12, 18], although Schottky junction devices with comparable performance have also been demonstrated using PbS[16] and PbSe[19, 20] QDs. The most common QDPV device architectures are shown in Figure 1.6.

■ 1.6 The Absorption-Collection Trade-off

Despite rapid advances in device performance and in the understanding of surface phenomena in colloidal QD films, contemporary QDPVs remain limited by a fundamental trade-off between light absorption and charge collection, which occur coaxially in a planar architecture. To allow full light absorption, the photoactive layer must be thicker than the absorption length L_{abs} of $\sim$1 μm, which assumes two optical passes through the QD film and a typical above-bandgap absorption coefficient α of 1×10^4 cm^{-1}[8]:

$$I(x,\omega) = I_0 e^{-\alpha(\omega)x} \tag{1.1}$$

To allow efficient carrier extraction, however, a planar PbS QD film must be thinner than the $\sim$250 nm carrier collection length L_{col}, which corresponds to the sum of the $\sim$150 nm *p*-side depletion width x_p and the $\sim$100 nm minority electron diffusion length

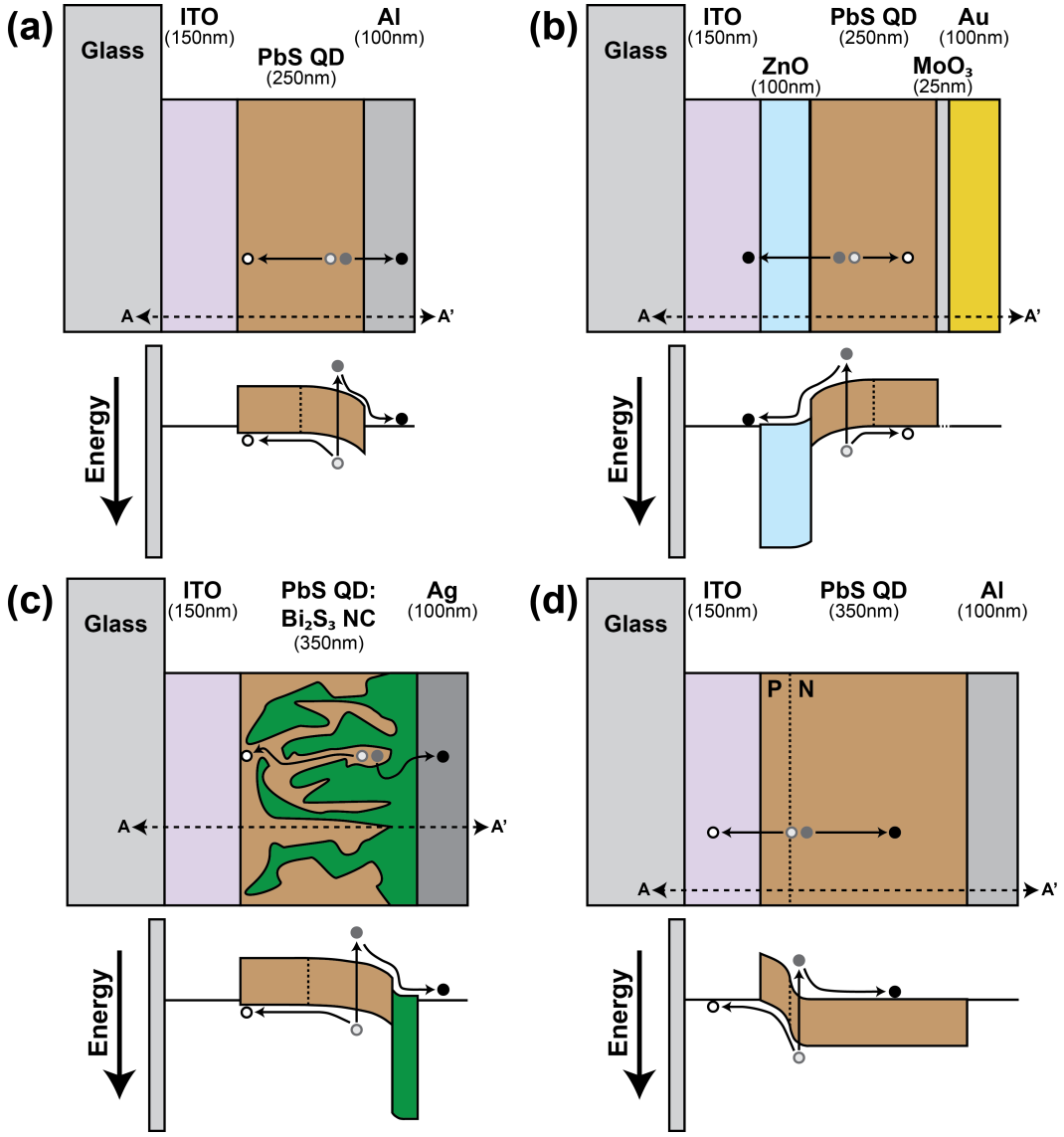

Figure 1.6: *Single-junction QDPV device architectures. Schematics and energy band diagrams at short-circuit (cross-sections along A-A') for (a) Schottky junction between PbS QDs and Al[11], (b) planar heterojunction between PbS QDs and ZnO[17], (c) bulk heterojunction between PbS QDs and Bi_2S_3 nanocrystals[21], and (d) homojunction with PbS QDs[22]. All film thicknesses are approximate.*

$L_{dif,n}$[23]:

$$L_{col} = x_p + L_{dif,n} \tag{1.2}$$

$$x_p = \sqrt{\frac{2\epsilon_p\epsilon_n\left(V_{bi} - V_a\right)}{q}\left(\frac{N_D}{N_A}\right)\left(\frac{1}{\epsilon_p N_A + \epsilon_n N_D}\right)} \tag{1.3}$$

$$L_{dif,n} = \sqrt{D_n\tau_n} = \sqrt{\frac{k_B T}{q}\mu_n\tau_n} \tag{1.4}$$

where ϵ_p and ϵ_n are the dielectric constants of the p-type and n-type materials, V_{bi} and V_a are the built-in and applied voltages, q is the electron charge, N_A and N_D are the acceptor and donor concentrations, D_n is the electron diffusion coefficient, τ_n is the minority electron lifetime, k_B is the Boltzmann constant, T is the operating temperature, and μ_n is the electron mobility. Note that the total heterojunction depletion width W_{dep} is equal to the sum of the depletion widths on the p- and n-type sides of the junction (x_p and x_n, respectively):

$$x_n = \sqrt{\frac{2\epsilon_p\epsilon_n\left(V_{bi} - V_a\right)}{q}\left(\frac{N_A}{N_D}\right)\left(\frac{1}{\epsilon_p N_A + \epsilon_n N_D}\right)} \tag{1.5}$$

$$W_{dep} = x_p + x_n = \sqrt{\frac{2\epsilon_p\epsilon_n\left(V_{bi} - V_a\right)}{q}\left(\frac{1}{N_A} + \frac{1}{N_D}\right)\left(\frac{N_A + N_D}{\epsilon_p N_A + \epsilon_n N_D}\right)} \tag{1.6}$$

These conflicting constraints on the active film thickness force us to sacrifice either absorption or collection in a planar device architecture (Figure 1.7).

The absorption-collection trade-off presents two clear paths forward for improving QDPV performance:

1. Improve absorption and decrease the film thickness to efficiently collect carriers.

2. Improve collection and increase the film thickness to fully absorb incoming light.

■ 1.6.1 Absorption Enhancement

We can enhance absorption by using plasmonic nanostructures to increase the effective optical path length in the QD film[24]. Such photon-management techniques can help reduce material requirements in solar cells with already-efficient charge collection; introduced directly in QDPVs, they could potentially double output photocurrents and efficiencies without any further advances in device design.

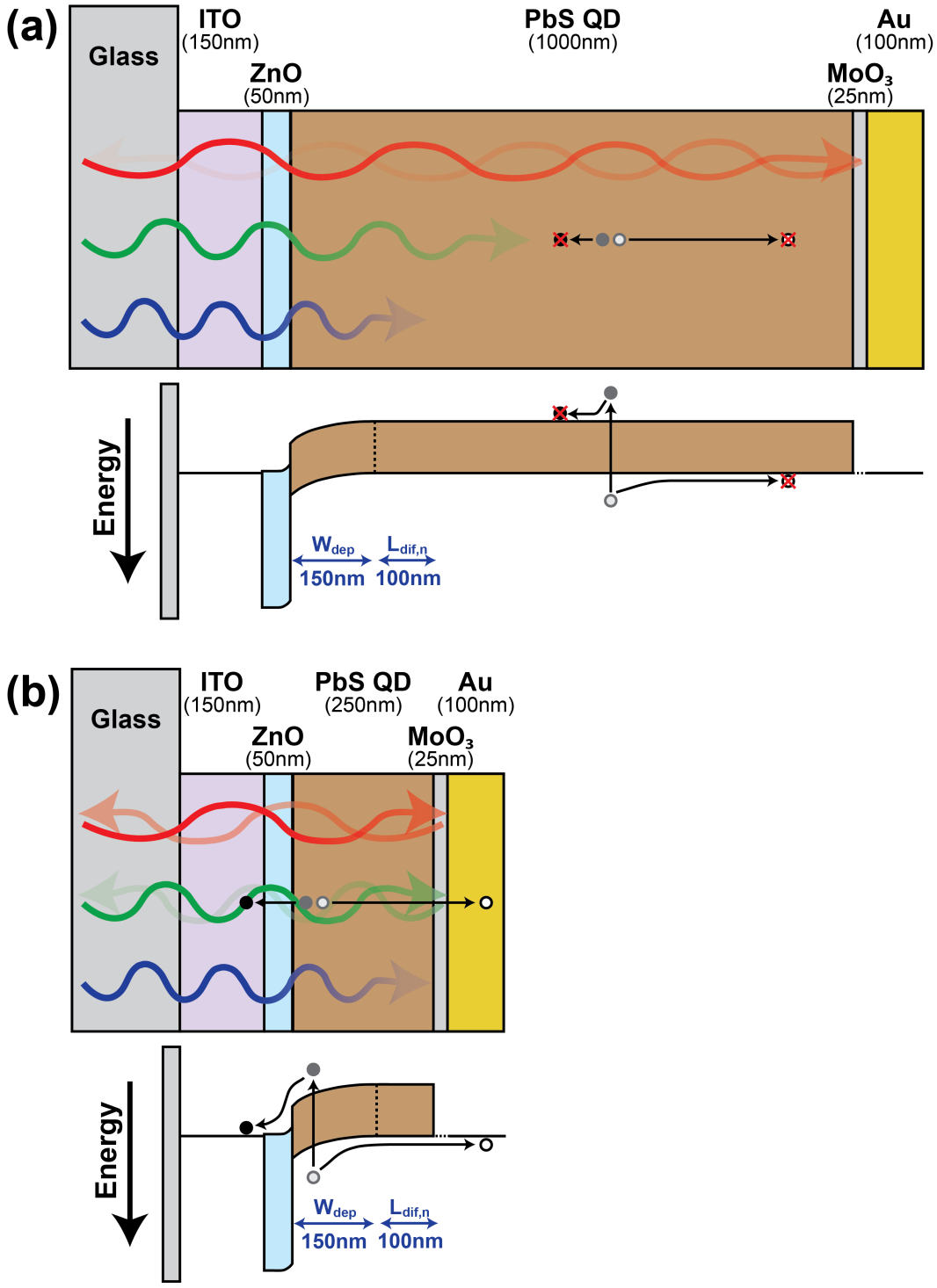

Figure 1.7: *The absorption-collection trade-off. (a) A thick QD active layer absorbs light fully but limits the extraction of photogenerated carriers. (b) A thin QD layer allows most photogenerated charge to be collected but absorbs only a fraction of the incident light.*

■ 1.6.2 Carrier Collection Enhancement

Alternatively, we can improve carrier collection by controlling how and where photogenerated carriers move in a QD solar cell. After a photon is absorbed and free carriers generated, charge extraction relies on the built-in field in the depletion region. The depletion width in a p-type semiconductor varies inversely with the square root of the acceptor dopant density (Equation (1.3)). Since doping in PbS QD films is suspected to arise from surface trap states[8], nonstoichiometric surface compositions and incomplete passivation yield a high hole density and therefore a short depletion width.

In an interface engineering approach, functional ligands are chosen to passivate QD surface states more completely, increasing both the depletion width and the diffusion length (Figure 1.8). A variety of organic[20, 25, 26], inorganic[27, 28, 29], and hybrid[12] ligand passivation approaches have already been attempted, but reported QD film thicknesses remain far below the ∼1 μm needed for complete absorption.

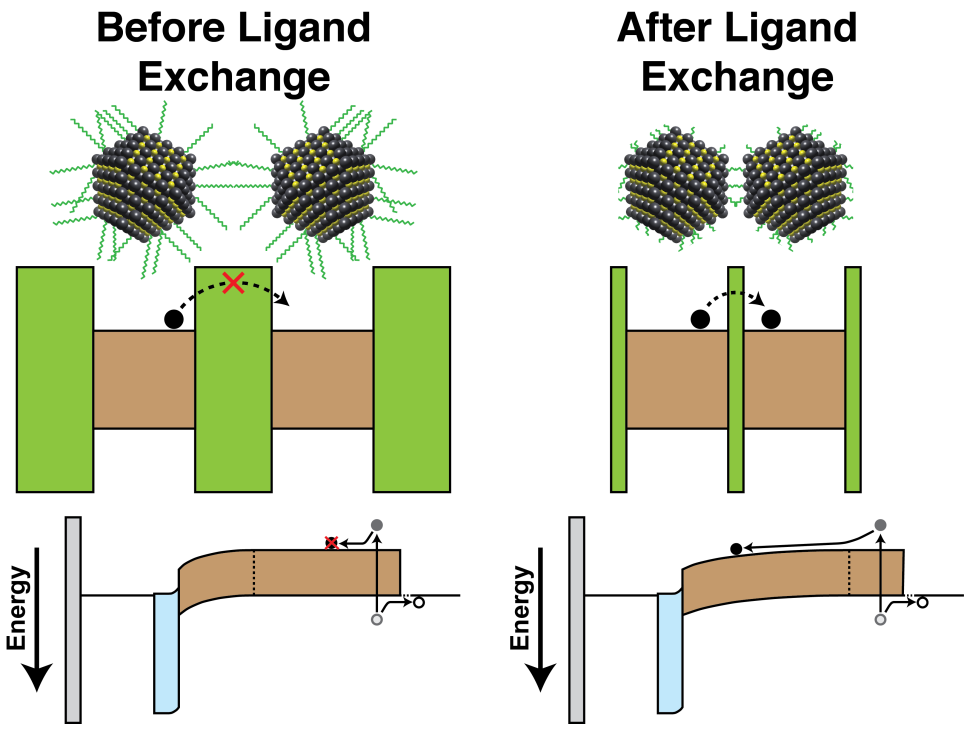

Figure 1.8: *Interface engineering to enhance charge carrier collection in QDPVs. Exchanging the long native capping ligands for shorter ligands brings adjacent QDs closer together and improves charge transport through QD films. Enhanced surface passivation widens the depletion region, thus increasing the collection length and further improving QDPV performance.*

■ 1.7 Architecture Engineering

In this work, we instead seek to improve collection efficiency through architecture engineering. The bulk heterojunction (BHJ) architecture (Figure 1.6c) has proven effective for polymer and small-molecule organic solar cells, in which short exciton diffusion lengths (∼tens of nanometers) similarly constrain charge extraction[30, 31]. In QD solar cells, a nanostructured active layer can increase the effective depletion width by forming a disordered or an ordered bulk heterojunction. Disordered BHJs rely on the intermixture of two interpenetrating phases, e.g., PbS QDs with Bi_2S_3 nanocrystals[21] or TiO_2 nanoparticles[32]. The blended active layer must therefore be optimized as a whole, and effective phase separation may be difficult. Furthermore, labyrinthine charge transport pathways and abundant heterojunction interfaces may hinder effective carrier extraction in disordered BHJs.

Due to these limitations on disordered BHJs, we focus instead on the ordered bulk heterojunction architecture. An ordered bulk heterojunction with vertically oriented 1-D nanostructures is the optimal device architecture for decoupling light absorption and carrier collection. The next chapter describes the experimental realization of an ordered BHJ quantum dot solar cell.

Chapter 2

The Ordered Bulk Heterojunction Architecture

THE ordered bulk heterojunction solar cell architecture consists of interdigitated electron- and hole-transporting layers that together form vertically aligned heterojunction interfaces. Since the two heterojunction materials are deposited sequentially rather than concurrently, the photoactive QD film and the nanostructured underlayer can be optimized more independently than in a disordered BHJ.

Most demonstrations of quantum dot solar cells incorporating 1-D nanostructures have focused on liquid-electrolyte photoelectrochemical cells in which TiO_2 nanotubes[33] or ZnO nanowires (NWs)[34, 35] are sensitized with a thin layer of cadmium chalcogenide QDs.

We focus here on solid-state ordered BHJ devices, in which vertically oriented 1-D nanostructure arrays are fully infiltrated with QDs, orthogonalizing the mechanistic length scales of light absorption and carrier collection—light is absorbed in the QD film parallel to the long nanowire axis, while electrons are collected laterally at a nearby heterojunction interface.

Solid-state ordered BHJ devices have been demonstrated with PbSe QDs and bottom-up-grown ZnO nanowires[36], as well as with PbS QDs and both top-down[37] and bottom-up[38] TiO_2 nanostructures. In contrast to top-down synthetic techniques such as lithographic patterning[39] or nanoimprint molding[40], bottom-up solution growth[41, 42, 43] may enable scalable, large-area production of 1-D nanostructures[44] on various electrode materials[45] for QD solar cell applications. We note that pursuing an architecture engineering approach does not preclude the advantages of interface engineering; improved surface passivation strategies can potentially be combined with 1-D nanostructured QDPV architectures to further enhance carrier transport and extraction.

Here we demonstrate an ordered bulk heterojunction QD solar cell with the device architecture shown in Figure 2.1a: tin-doped indium oxide (ITO) / ZnO seed layer / ZnO nanowires / PbS QDs / MoO_3 / Au. The corresponding model band diagram is shown in Figure 2.1b. As detailed in the following sections, we grow ZnO nanowires by a simple hydrothermal process and optimize several synthetic parameters to achieve maximum crystal quality, vertical alignment, and large-area uniformity. Nanowire-based QDPV devices are then fabricated and used to demonstrate the increased importance of a MoO_3 anode interlayer for 1-D nanostructured devices (see Chapter 3)[46]. Optimization of the ZnO nanowire growth process and the NW-QDPV device architecture yields a 50% enhancement in short-circuit current density and a 35% enhancement in power conversion efficiency over optimized planar devices. Our NW-QDPV devices achieve an average spectral mismatch-corrected efficiency of $(3.7 \pm 0.2)\%$ and a maximum efficiency of 4.9%, among the highest efficiencies reported to-date for QD solar cells based on ZnO[17, 18, 47, 48]. Along with the recent demonstration of titania nanopillar-based QDPVs by Kramer *et al.*[37], our study suggests that 1-D nanostructures may point the way forward for enhanced performance in colloidal quantum dot solar cells.

■ 2.1 Bottom-up Growth of ZnO Nanowires

We focus on solution-grown ZnO nanowire arrays as an electron-transporting layer for several reasons:

1. ZnO is one of the two primary wide-bandgap n-type semiconductors used in conjunction with PbS QDs in planar heterojunction QDPVs (the other is TiO_2).

2. Solution-processed ZnO nanostructures have been studied extensively in the literature, and they can be grown over large areas and on arbitrary substrates, including silicon, polydimethylsiloxane (PDMS), thermoplastic polyurethanes (TPU), paper, and organic fibers (see review by Xu *et al.*[43]). Such processing versatility complements the advantages of QDPVs and other nanomaterial-based PV technologies.

3. Vertically aligned and defect-free ZnO nanowires can be grown in aqueous solutions without the use of metal catalysts, which could otherwise introduce material incompatibilities and additional processing complexity.

The ZnO nanowire growth process consists of two primary steps: deposition of a planar ZnO seed layer, followed by hydrothermal nanowire growth in an aqueous solution.

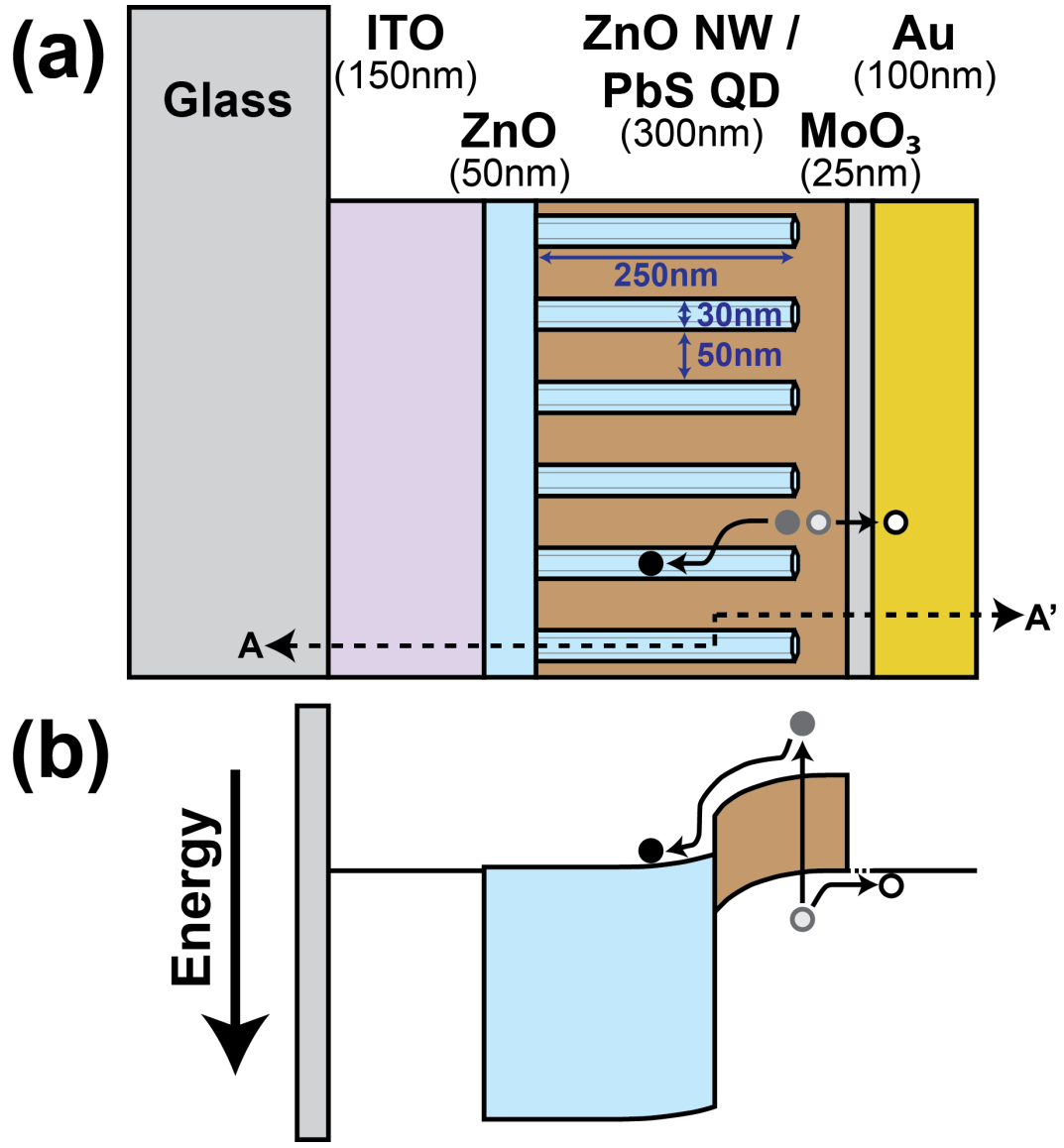

Figure 2.1: *The ordered bulk heterojunction QDPV architecture. By incorporating solution-processed ZnO nanowires, an ordered BHJ architecture—shown here by: (a) schematic and (b) energy band diagram (cross-section along A-A')—can decouple absorption from collection, extending the effective depletion width throughout a thick QD film.*

■ 2.1.1 Seed Layer Deposition

A nanocrystalline ZnO seed layer can provide a starting point for heterogeneous nucleation and subsequent nanowire growth, divorcing nanowire properties from the nature of the underlying substrate. Using seeds effectively divides the nanowire growth process into two steps: homogeneous nucleation to form the planar seed layer—either colloidal nanocrystals or a dense film—followed by heterogeneous growth to form vertical nanowires. Since the activation energy and hence the required precursor supersaturation levels are lower for heterogeneous nucleation than for homogeneous nucleation[43], precursor ions in the growth solution preferentially nucleate on a seeded substrate instead of forming homogeneous precipitates or accumulating on unseeded surfaces.

We start with patterned ITO-coated glass or silicon substrates and deposit a thin ($\sim$50 nm) film of ZnO via radio-frequency magnetron sputtering[49] or sol-gel[50] methods. In typical QDPV devices, planar ZnO is the sole electron-transporting layer, while in nanowire-based QDPVs, it serves primarily as the seed layer for nanowire growth. Amorphous sputtered ZnO films are more consistent in thickness and electronic behavior, but we find that polycrystalline sol-gel films produce better-aligned nanowire arrays, likely due to the $\langle 0001 \rangle$-alignment of the individual seed crystals[50].

To prepare the sol-gel precursors, solutions of zinc acetate dihydrate (300 mM) and ethanolamine (300 mM) in 2-methoxyethanol are mixed in equal proportion and ultrasonicated for 20 minutes. This mixture is then spin-cast at 4000 rpm and annealed at 175 °C for 10 minutes in air, with two spin-anneal cycles needed to form a uniform and complete film. We characterized the sol-gel ZnO film morphology using tapping-mode atomic force microscopy (AFM), finding an average grain size of 46 nm and a RMS surface roughness of 1.3 nm (Figure 2.3).

■ 2.1.2 Hydrothermal Nanowire Growth

We grow vertically aligned arrays of ZnO nanowires on nanocrystalline sol-gel seed layers via an established hydrothermal procedure[41, 50, 51]. Silicon or ITO-coated glass substrates with sol-gel ZnO seed layers are floated facedown in an aqueous bath containing equal volumes of zinc nitrate hexahydrate (50 mM) and hexamethylenetetramine (HMTA, 50 mM) in deionized (DI) water at 90 °C. After a growth period lasting from 30 minutes to 2 hours (see Figure 2.6 for growth curve), the substrates are thoroughly rinsed with DI water, dried under flowing nitrogen, and annealed on a hot plate at 200 °C for 5 minutes. A scanning electron microscope (SEM) image of a representative ZnO nanowire

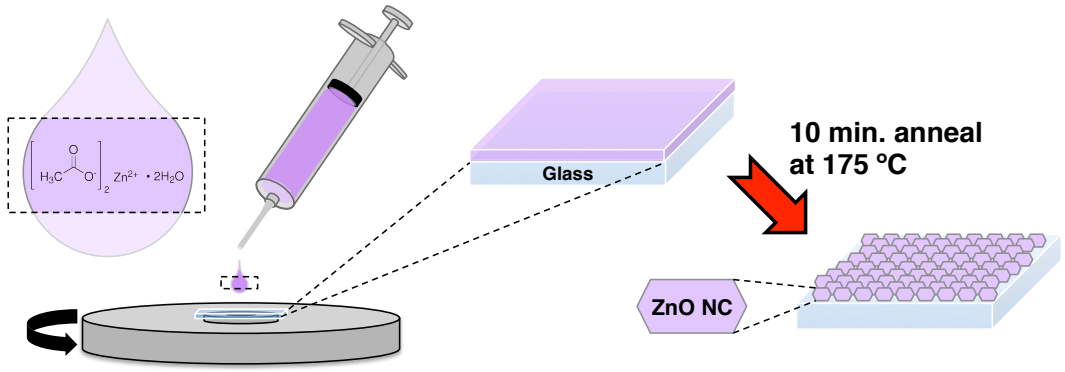

Figure 2.2: *Procedure for sol-gel preparation of ZnO seed layer. Solutions of zinc acetate (precursor), ethanolamine (additive), and 2-methoxyethanol (solvent) are spin-cast and annealed at 175 °C for 10 minutes to form a dense nanocrystalline ZnO film. Multiple spin-anneal cycles allow deposition of thicker films.*

array is shown in Figure 2.5. All SEM imaging was performed using an FEI Helios NanoLab 600i in immersion mode at 5 kV.

■ 2.2 Characterization of ZnO Nanowire Arrays

To refine the nanowire growth process and prepare arrays suitable for QDPV devices, we first establish criteria for assessing nanowire quality. One such criterion is the vertical array ordering, which is strongly affected by the morphology of the underlying seed layer. Vertically aligned nanowires allow direct electron transport to the cathode and hole transport to the anode, reducing the probability of electron back-transfer and recombination. Another criterion for evaluating nanowire arrays is the large-area uniformity, which is of particular concern for bottom-up growth processes. Stochastic variations in nanowire areal density translate to non-uniform QD film thicknesses and quasi-neutral region widths across the device area. Furthermore, fluctuations in nanowire length manifest as either low shunt resistance or high series resistance: Long nanowires create shunting pathways and increase the reverse leakage current, while short nanowires cannot fully deplete the QD film and thus incur recombination losses.

To obtain a reproducible model nanowire system for further studies, we independently optimized several synthetic parameters—seed layer thickness, seed layer annealing time and temperature, and nanowire growth time—with the goal of generating single-crystalline nanowires with consistent vertical ordering and large-area uniformity (see Figures 2.6 and 2.7). Other key parameters—including precursor chemistry, precursor

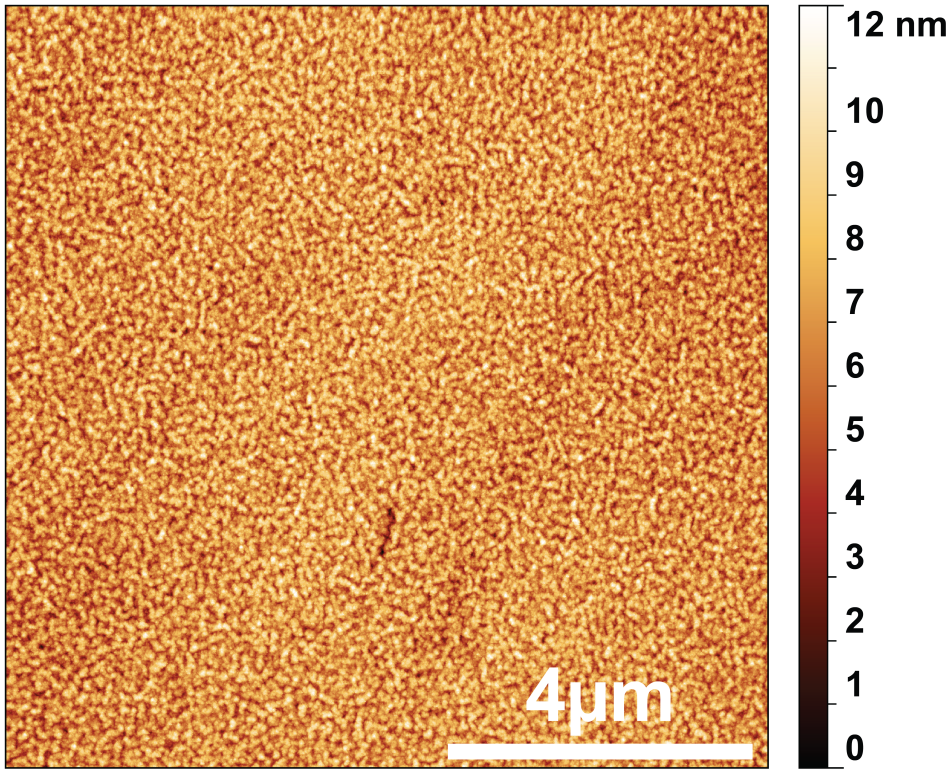

Figure 2.3: *AFM image of a planar sol-gel ZnO film. Individual crystalline grains have an average diameter of 46 nm, and the RMS surface roughness of the film is 1.3 nm.*

concentrations, and growth temperature—were chosen according to established literature methods[41, 50, 51].

We confirmed the nanowire crystal quality, alignment, and uniformity through photoluminescence (PL) measurements, scanning electron microscopy, and transmission electron microscopy (TEM). The absence of a yellow-orange (∼570 nm) peak in the PL spectrum (Figure 2.8)—typically associated with interstitial oxygen ions[52]—suggests that the nanowires have few atomic defects[44]. Scanning electron micrographs clearly show vertical array alignment (Figure 2.6) and hexagonal cross-sections (Figure 2.5), suggestive of single-crystalline wurtzite ZnO.

Bright-field transmission electron micrographs (Figure 2.9) confirm lattice spacings of 5.2 Å and 2.8 Å in the $\langle 0110 \rangle$ and $\langle 01\bar{1}0 \rangle$ directions, respectively, consistent with the known lattice constants of wurtzite ZnO. TEM analysis was performed using a JEOL 2010F FEG analytical TEM at 200 kV, and low-magnification images were obtained

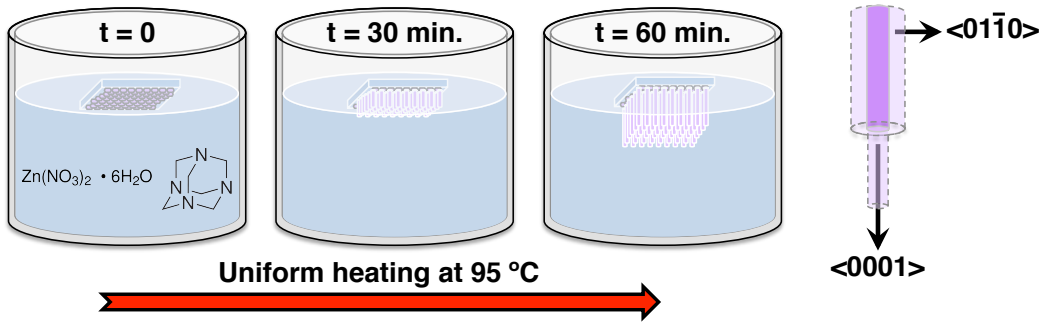

Figure 2.4: *Procedure for hydrothermal growth of ZnO nanowires. Substrates coated with ZnO seed films are floated facedown in an aqueous bath of zinc nitrate and HMTA and heated to 90 °C for a growth period of up to 2 hours, yielding ordered arrays of single-crystalline* $\langle 0001 \rangle$*-oriented nanowires.*

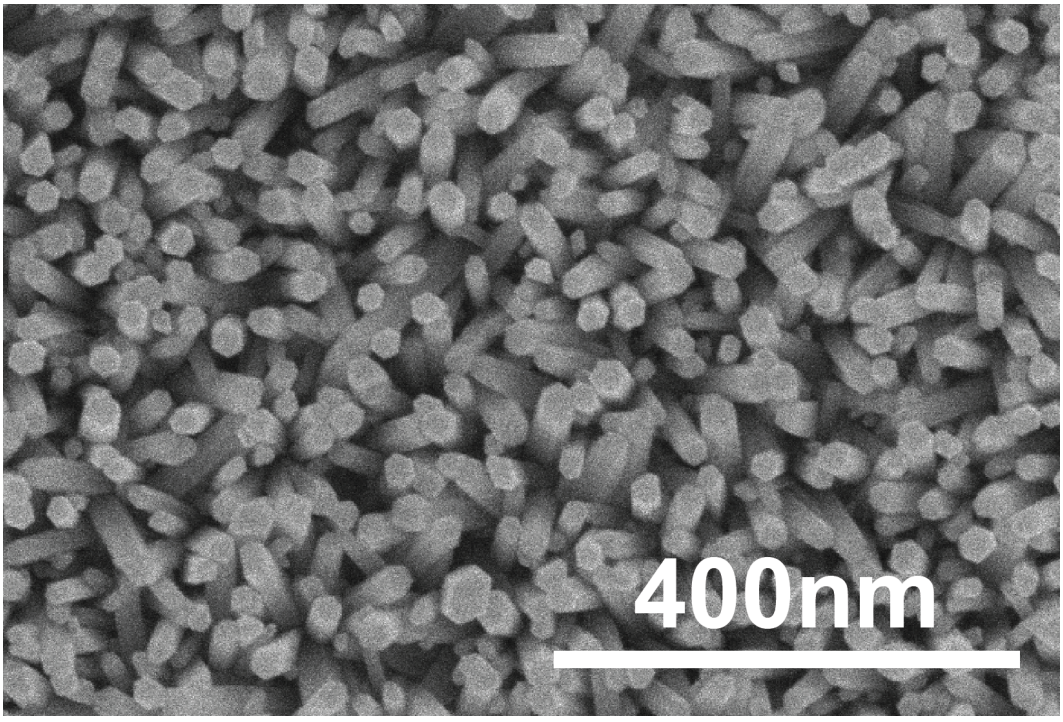

Figure 2.5: *SEM image of a ZnO nanowire array grown by a seeded hydrothermal process. The areal density of 200-400 nanowires* μm^{-2}*—along with an average diameter of 20-30 nm—yields an average spacing between adjacent nanowires of 30-50 nm.*

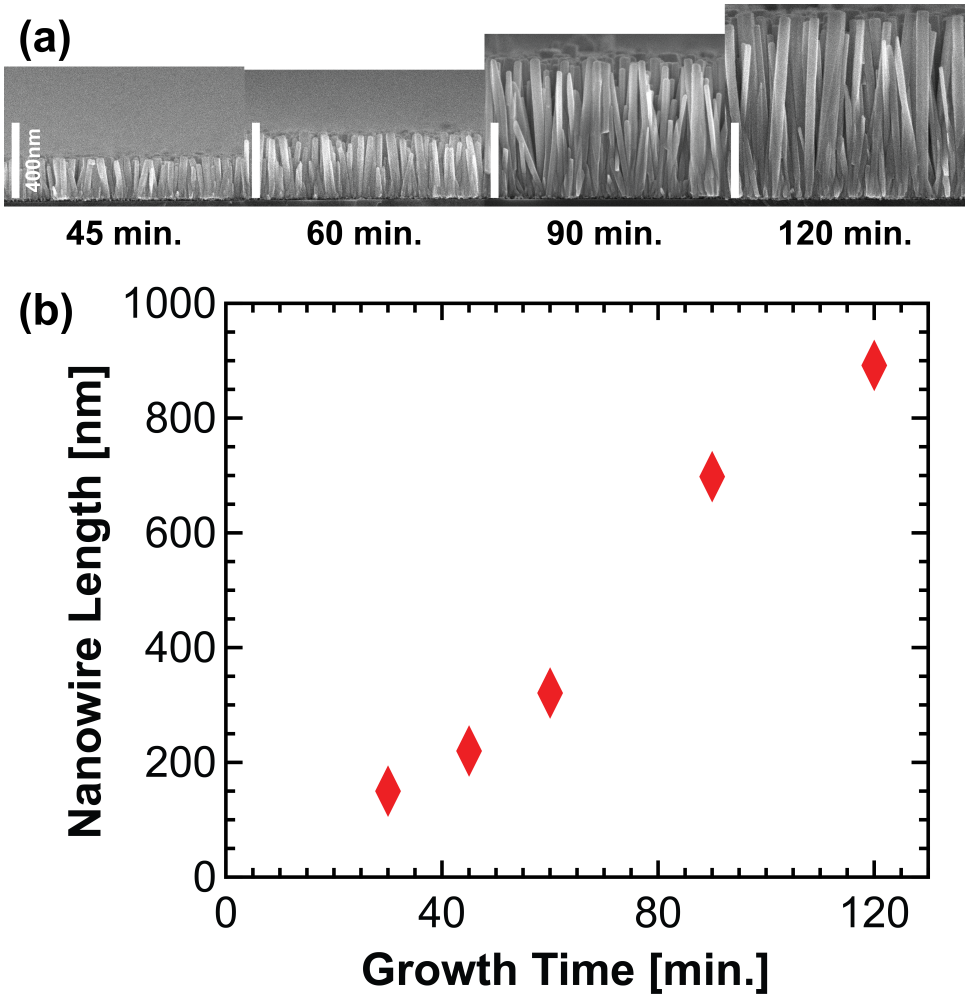

Figure 2.6: *Variation in ZnO nanowire length with growth time. (a) Cross-sectional SEM images of ZnO nanowire arrays grown on sol-gel ZnO on Si substrates, with growth times varying from 45 minutes to 2 hours. (b) A plot of average nanowire length vs. growth time reveals a linear growth regime between 30 and 60 minutes, yielding lengths of up to 320 nm. Nanowires with lengths of 200-250 nm were used in this work. Average lengths vary predictably with time, with a run-to-run error of ∼10 nm. ZnO nanowire arrays grown on ITO follow a similar growth trend.*

using an objective aperture to enhance contrast. From SEM analysis, we estimate an areal density of 200-400 nanowires μm^{-2}, an average diameter of 20-30 nm, an average length of 200-250 nm, and an average inter-nanowire spacing of 30-50 nm near the top of the array.

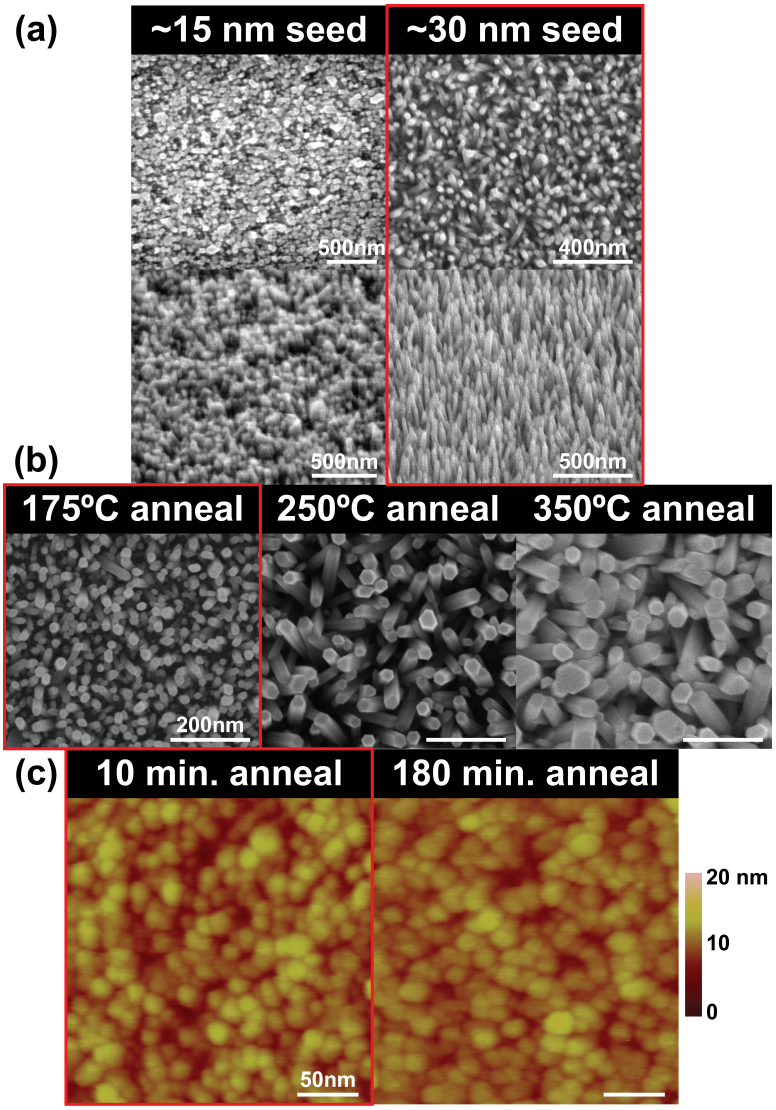

Figure 2.7: *Optimization of ZnO nanowire growth. SEM and AFM analysis reveals the effect of several synthetic parameters on ZnO nanowire crystallinity, morphology, alignment, and uniformity. The parameter values ultimately used in this work are outlined in red. (a) Plan-view (top) and tilted (bottom) SEM images of nanowire arrays grown on seed layers of varying thickness. The seed layer thickness affects the length, aspect ratio, and uniformity of nanowire arrays. Nanowires grown on a ∼15 nm thick seed layer (1 spin) exhibit a low aspect ratio and highly non-uniform tip morphology and length, while nanowires grown on a ∼30 nm thick seed layer (2 spins) exhibit uniform lengths, diameter, and morphology. (b) Plan-view SEM images of nanowire arrays grown on seed layers annealed at different temperatures. The seed layer annealing temperature affects the diameter, alignment, density, and pitch of nanowire arrays. Higher temperatures yield nanowires with increased diameter and polydispersity, reduced vertical alignment, and reduced areal density. (c) AFM images of ZnO seed layers annealed for different durations. The seed layer annealing time does not significantly affect the morphology of the sol-gel-derived ZnO seeds. Seed layers annealed at 150 °C for 10 minutes or 180 minutes exhibit minimal differences in grain height (3-4 nm) and RMS surface roughness (1.3-1.7 nm).*

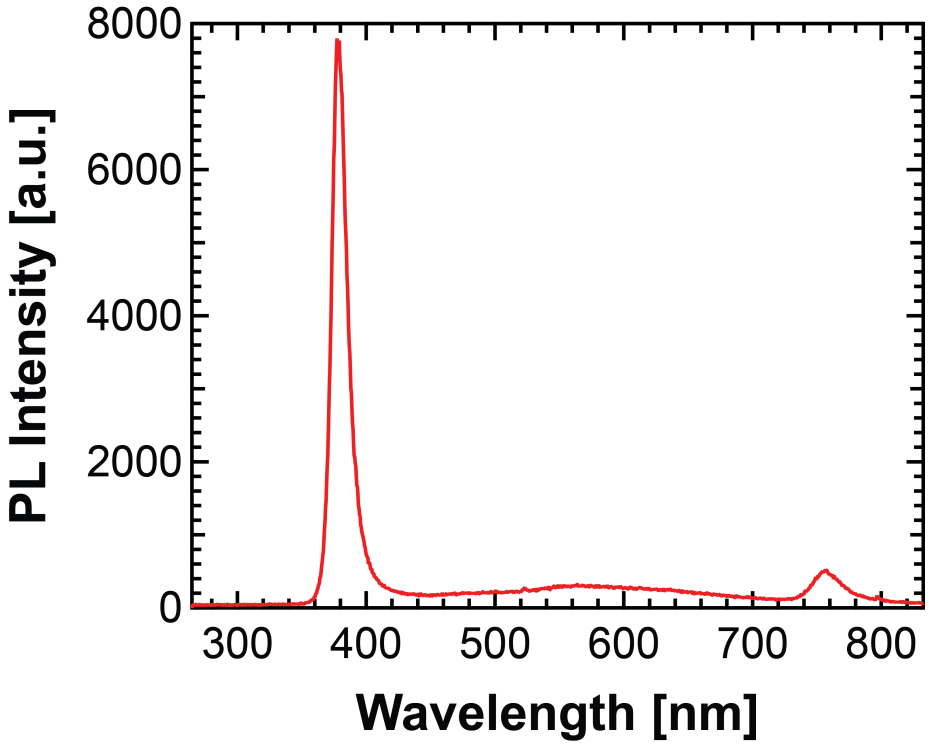

Figure 2.8: *Photoluminescence (PL) spectrum of a hydrothermally-grown ZnO nanowire array. The low PL signal at ∼570 nm relative to the band edge emission at 378 nm confirms the low density of interstitial oxygen ions and hence a high proportion of defect-free, single-crystalline nanowires. The small additional peak at 756 nm corresponds to second-order transmission of the band edge signal.*

■ 2.3 Fabrication of Nanowire-QD Solar Cells

To fabricate a complete ordered BHJ device, we start with patterned ITO-coated glass substrates cleaned by successive ultrasonication in alkaline cleaning solution, DI water, and acetone, followed by immersion in boiling isopropanol for 5 minutes. The substrates are then dried under flowing nitrogen and exposed to oxygen plasma for 30 s to remove organic contaminants.

After ZnO seed layer deposition and nanowire growth, multilayer PbS QD films are deposited by sequential layer-by-layer spin-casting (Figure 2.10). Each layer consists of three steps: QD deposition, ligand exchange, and solvent rinse. Two drops (∼20 μL) of PbS QD solution (25 mg mL^{-1}) in octane are spin-cast for 10 s at 1500 rpm. Ten drops (∼100 μL) of a 1,3-benzenedithiol (BDT) solution (1.7 mM) in acetonitrile are then dropped onto the substrate and spun dry after a 30 s wait to ensure complete exchange

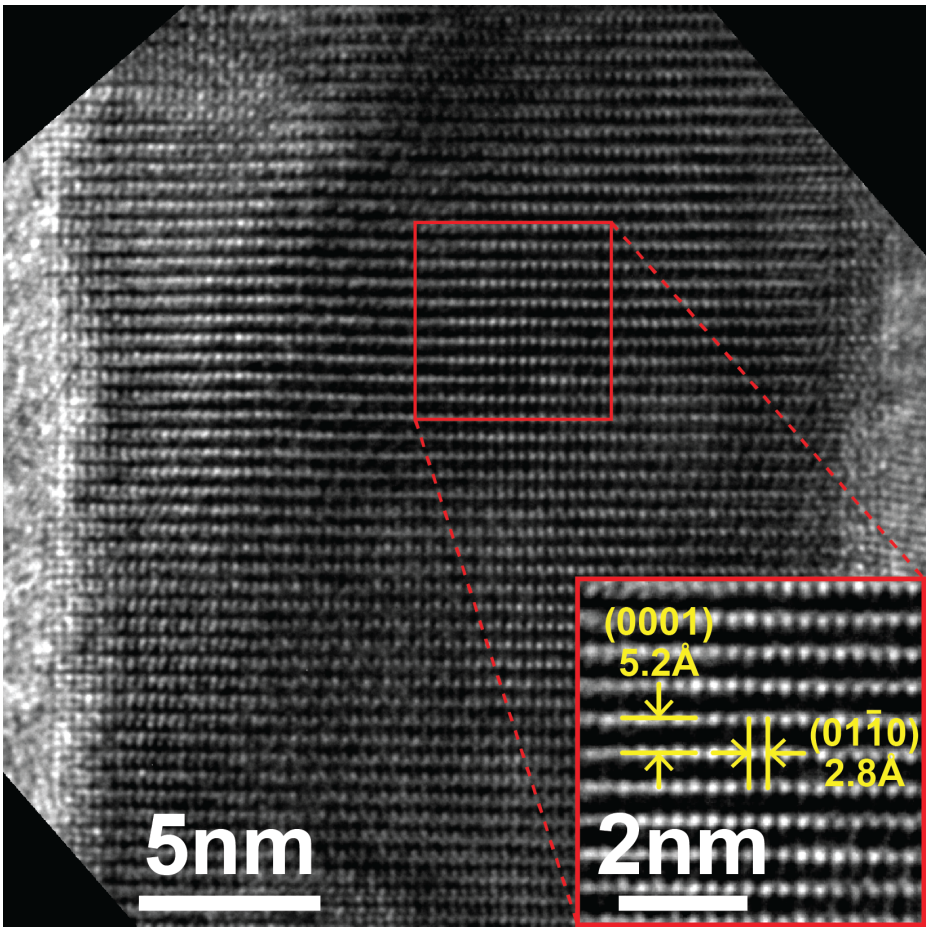

Figure 2.9: *Lattice-resolved bright-field TEM image of a* $\langle 0001 \rangle$*-aligned ZnO nanowire. The inset shows a magnified view along the* $\langle 2\bar{1}\bar{1}0 \rangle$ *zone axis, with measured lattice spacings of 5.2* Å *and 2.8* Å *in the* $\langle 0001 \rangle$ *and* $\langle 01\bar{1}0 \rangle$ *directions, respectively, consistent with known lattice constants of wurtzite ZnO.*

with the native oleic acid capping ligands. The substrate is rinsed three times with acetonitrile to remove excess ligands and spun dry. For a typical NW-QDPV device, this process is repeated 10 times, forming a QD film with a thickness of ∼250 nm. The PbS QD and BDT solutions are dispensed through a 0.1 μm PTFE membrane filter. Note that the PbS QDs used in this work exhibit a first excitonic absorption peak between 905 nm and 1150 nm, corresponding to an optical bandgap between 1.37 eV and 1.08 eV.

After QD deposition, a 25 nm MoO_3 buffer layer and 100 nm Au back contact are thermally evaporated through a shadow mask at rates of 0.5 Å s^{-1} and 1 Å s^{-1},

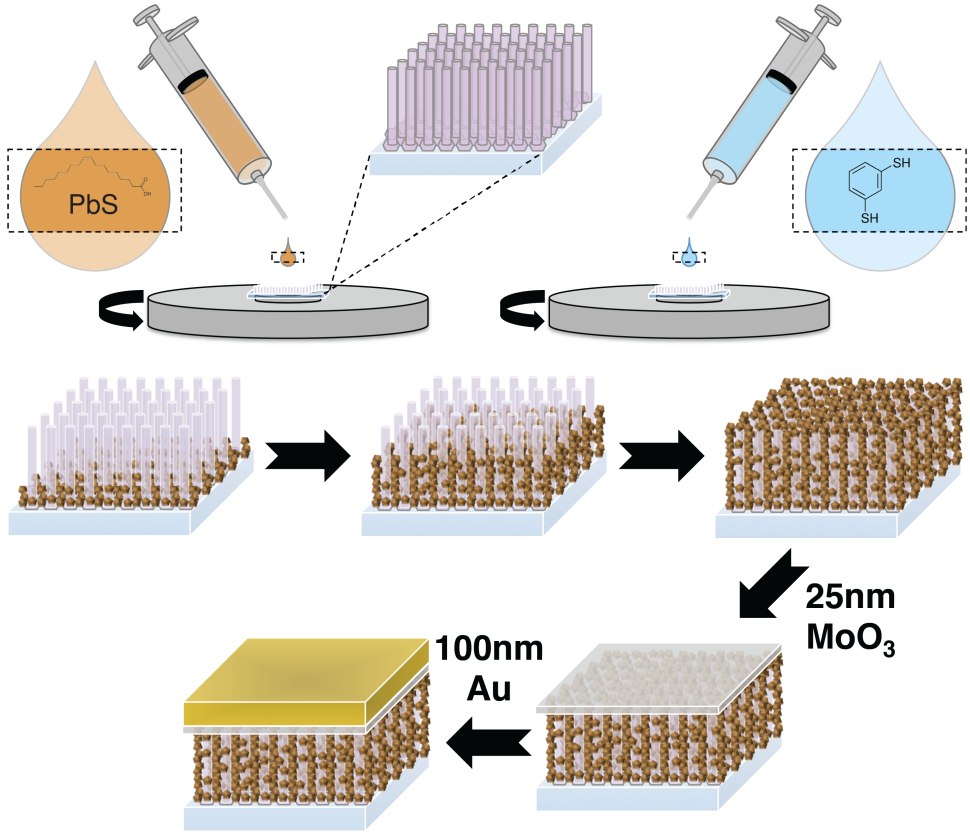

Figure 2.10: *NW-QDPV fabrication procedure. (a) PbS QD films are deposited onto ZnO nanowire arrays by sequential spin-casting to form an interdigitated bulk heterojunction. The native oleic acid capping ligands are exchanged for shorter BDT ligands during film formation. (b) A thin MoO_3 buffer layer and patterned Au back electrode are deposited by thermal evaporation through a shadow mask.*

respectively, and a base pressure of 1×10^{-6} Torr. The active device area is defined by the overlap of the Au anode with the ITO cathode to be either 1.21 mm^2 or 5.44 mm^2. Note that all processing steps after the ZnO nanowire growth are performed in inert N_2 atmosphere to minimize oxidation of the QDs and the organic capping ligands.

We find that fewer spin-casting cycles are needed to deposit a QD film of equivalent thickness on nanowire arrays than on planar films. Higher apparent deposition rates—24-29 nm per cycle, compared to ∼23 nm per cycle for planar devices (Figure 2.11)—can be attributed partly to incomplete QD infiltration into the array (see voids in Figure 2.12a) and partly to the additional volume occupied by the nanowires. Furthermore, instead of only accumulating upward from the seed layer—as on planar ZnO films—QDs

also accumulate radially on the nanowire side planes, increasing the volume of QDs deposited per cycle. In the limit of fully conformal deposition, the volumetric growth rate of thin films is proportional to the exposed surface area, which is much higher for nanostructured surfaces than for planar films. We find that the thickness of QDs deposited per spin cycle remains constant for planar ZnO but decreases monotonically with increasing total film thickness for nanowire arrays: Nanowire volume filling, partial voiding, and radial growth initially yield thicker layers, but after the nanowires are fully covered, the average thickness deposited per cycle approaches that on planar ZnO. Cross-sectional SEM and TEM analysis of complete nanowire-based QDPV devices, shown in Figure 2.12, indicates that the spin-cast QDs are in close proximity to the underlying nanowires after device fabrication.

In the next chapter, we characterize the photovoltaic behavior of ordered bulk heterojunction QD solar cells and explore the effect of various fabrication parameters and operating conditions on device performance.

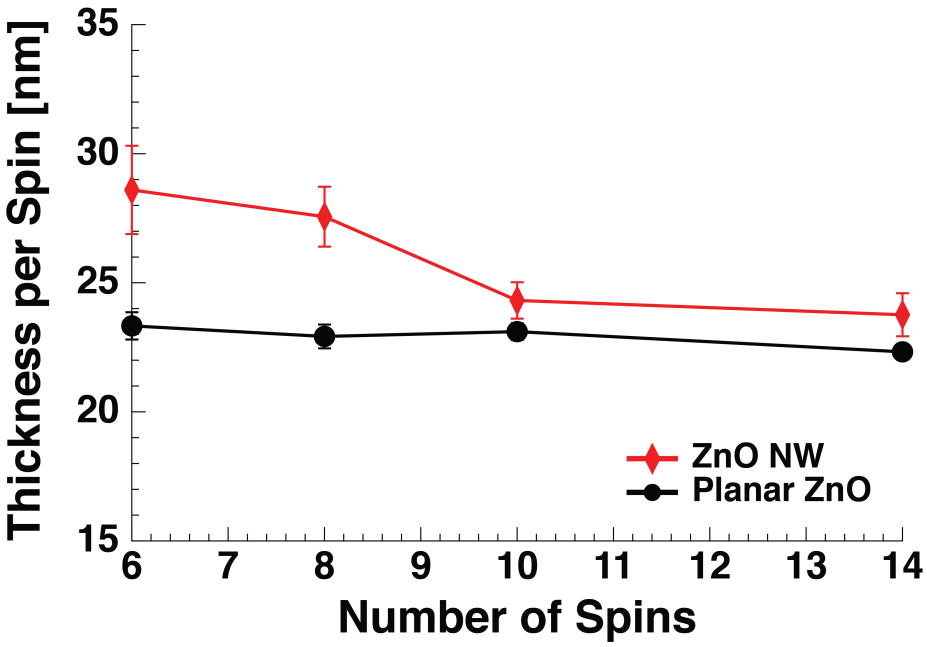

Figure 2.11: *Average thickness of PbS QDs deposited per spin on planar ZnO (black circles) and ZnO nanowire arrays (red diamonds). Nanowire volume filling, partial voiding, and radial growth initially yield thicker films per spin on the ZnO nanowire arrays; once the nanowires are fully covered, the average thickness per spin approaches that on planar ZnO. Note that the QD film thickness on nanowire arrays is measured from the deepest point of penetration apparent in cross-sectional SEM images taken over a 20 μm wide region.*

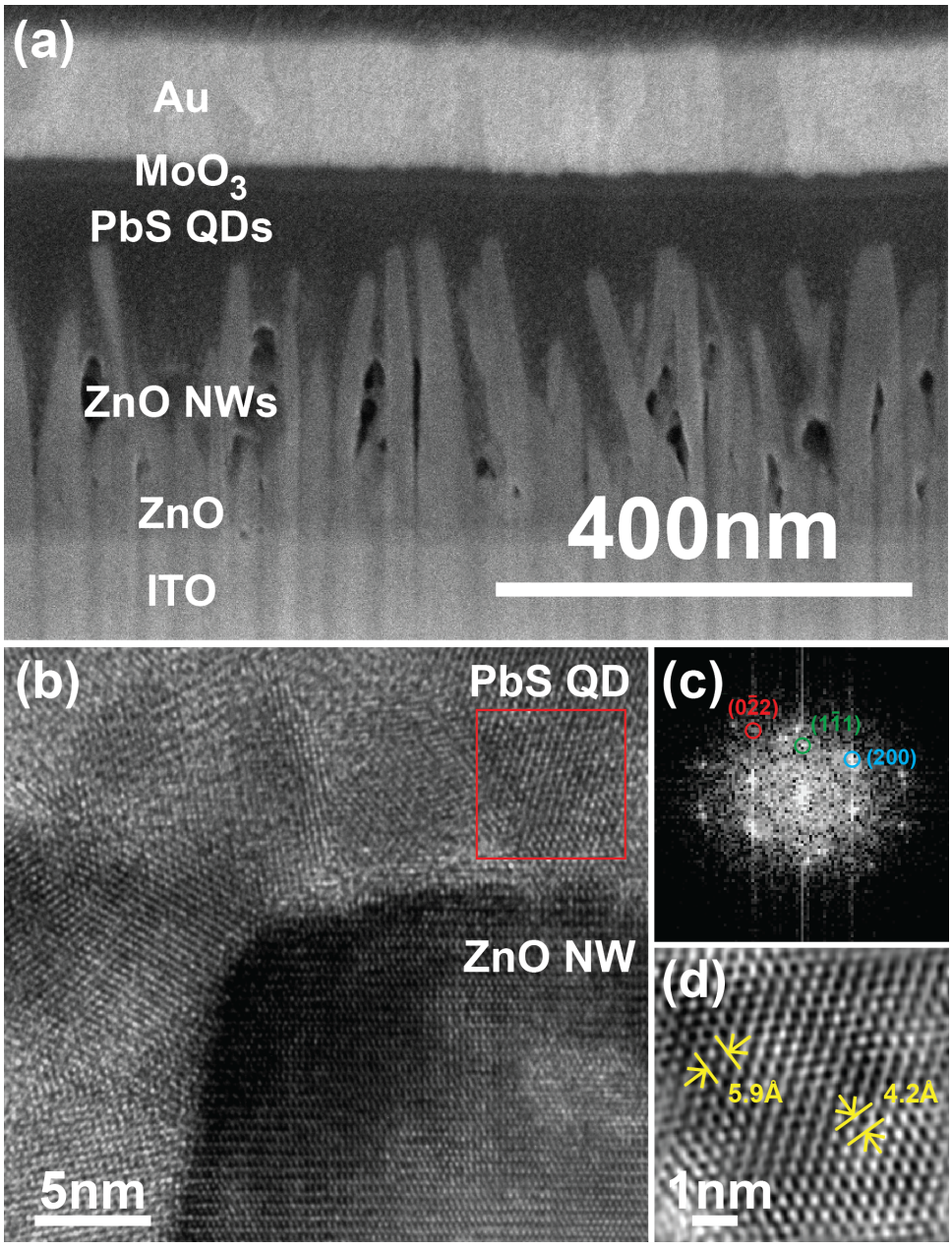

Figure 2.12: *Cross-sectional micrographs of representative NW-QDPVs. (a) SEM images reveal the vertical ordering of solution-grown ZnO nanowires. Voids near the base of the nanowires appear dark and indicate incomplete infiltration of PbS QDs into the dense nanowire array. (b) Lattice-resolved bright-field TEM analysis shows proximity of PbS QDs and the tip of a ZnO nanowire in a complete device. (c) The indexed FFT of the area defined by the red square in (b), which corresponds to an individual QD, reflects the simple cubic structure of PbS as viewed along the* $\langle 011 \rangle$ *zone axis. (d) The Fourier-filtered inverse FFT of (c) shows lattice spacings of 5.9 Å and 4.2 Å, consistent with known lattice constants of cubic PbS.*

Chapter 3

Characterization of Ordered Bulk Heterojunction QDPVs

WE find that the introduction of ZnO nanowire arrays can significantly boost the photocurrent and the power conversion efficiency of colloidal QD solar cells.

■ 3.1 Performance of Nanowire-QD Solar Cells

We perform basic current density-voltage (J-V) characterization of QD solar cells using a Keithley 6487 picoammeter, with 100 ± 10 mW cm^{-2} simulated solar illumination provided by a 150 W Newport 96000 xenon arc-lamp equipped with an AM1.5G filter and diffuser lens. Our typical NW-QDPV devices achieve a short-circuit current density of 14.9 ± 1.1 mA cm^{-2}, an open-circuit voltage of 0.60 ± 0.01 V, a fill factor of (40.5 ± 3.3)%, and a power conversion efficiency of (3.7 ± 0.2)% under AM1.5G illumination (averaged over 16 devices). The highest-performing devices on each substrate regularly exhibit efficiencies of up to 4.3%—a representative J-V curve is shown in Figure 3.1a—but non-uniformity across the nanowire array reduces the average device performance. All reported photocurrents and efficiencies are scaled by 0.853 to correct for spectral mismatch. A champion NW-QDPV device employing larger PbS QDs with a first excitonic peak at 1150 nm exhibits a short-circuit current density of 25.4 mA cm^{-2}, an open-circuit voltage of 0.51 V, a fill factor of 37%, and a maximum efficiency of 4.9% (Figure 3.1b).

External quantum efficiency (EQE) measurements allow us to characterize the spectral photoresponse of ordered BHJ devices. The spectral mismatch factor used here was derived by comparing measured photocurrents with predicted values from integration of the EQE against the AM1.5G spectrum. The representative EQE spectrum shown in Figure 3.2 reveals a 150% increase in EQE over planar devices at the red-shifted excitonic

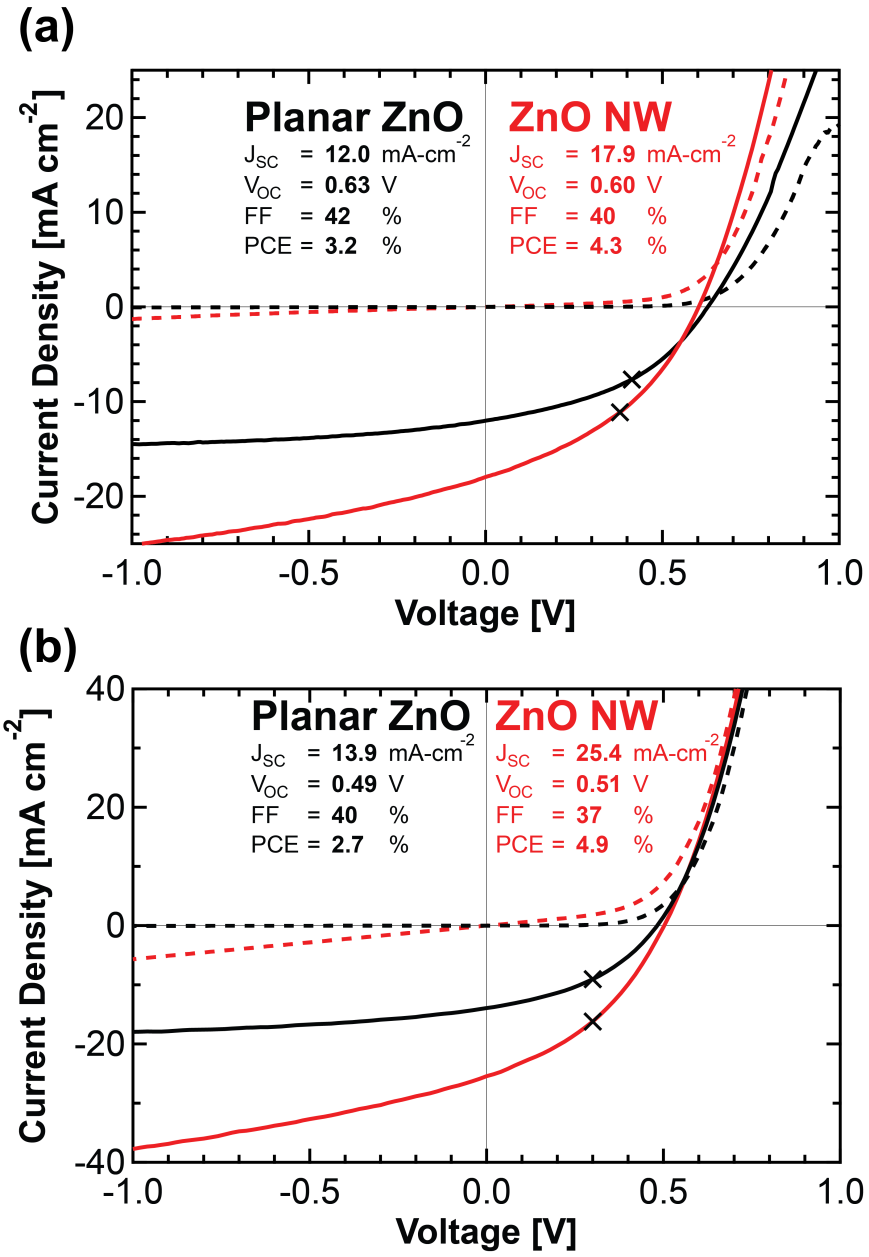

Figure 3.1: *Electrical characterization of nanowire-based QDPVs. (a) J-V characteristics measured in the dark (dashed) and under AM1.5G illumination (solid) for representative planar (black) and nanowire-based (red) QDPV devices using 905 nm (1.37 eV) PbS QDs and photoactive films of optimal thickness for each architecture. Each curve represents the average performance of 2-4 devices on a single substrate. Incorporation of ZnO nanowires boosts the short-circuit current density (J_{SC}) by 50% and the overall power conversion efficiency (PCE) by 35%, although a low shunt resistance decreases the fill factor (FF). (b) J-V characteristics of planar (black) and champion nanowire-based (red) QDPV devices employing PbS QDs with a first excitonic peak at 1150 nm (1.08 eV). A smaller QD band gap increases J_{SC} but decreases the open-circuit voltage (V_{OC}). Black crosses indicate the maximum power point.*

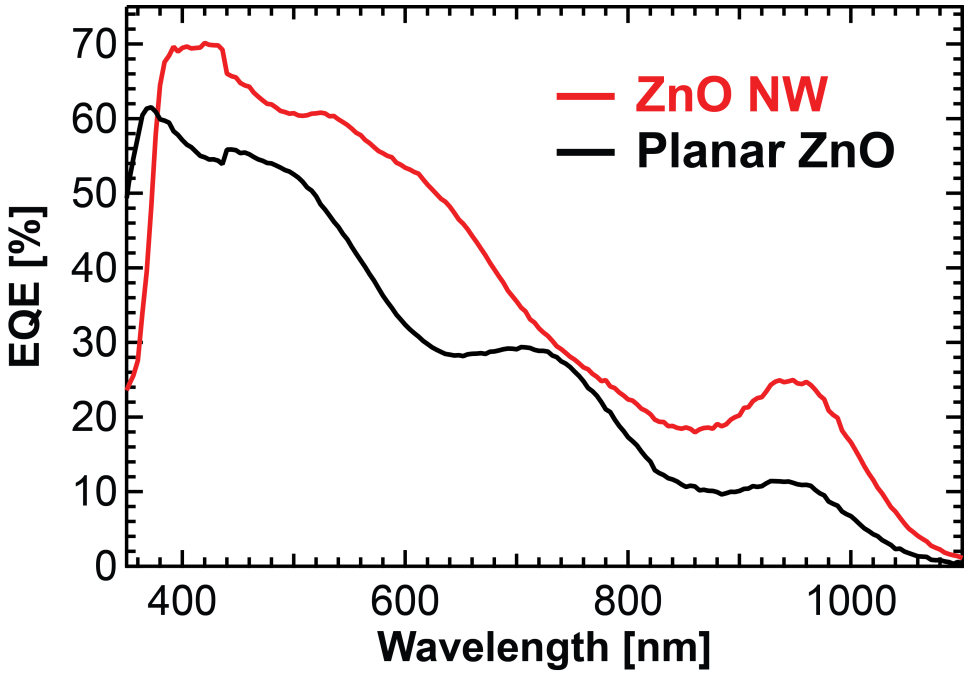

Figure 3.2: *External quantum efficiency (EQE) spectra of planar (black) and nanowire (red) devices. The inclusion of ZnO nanowires increases the EQE at the ∼930 nm excitonic peak by nearly 150%, indicative of improved collection efficiency for photocarriers generated far from the planar heterojunction interface. The slight discontinuity around 450 nm corresponds to differential drift upon changing the filter wheel used to eliminate higher-order illumination that passes through the monochromator in our measurement set-up. While this jump can be minimized by repeated recalibration during testing, the relatively low solar intensity below 450 nm yields a correction of less than 1% to the spectral mismatch upon manual offsetting.*

peak (at a wavelength of 930 nm). Since longer-wavelength photons are absorbed deeper in the photoactive film, this boost in the near-infrared EQE suggests that nanowires are most helpful for collecting electrons generated in the region of the QD film closest to the back contact.

We note that all EQE spectra were measured without bias illumination. The responsivity of nanowire and planar devices remains roughly constant with light intensity (Figure 3.3), which suggests that the corresponding EQE measurements should not depend strongly on bias illumination. Furthermore, while no aperture was employed during J-V characterization, our use of underfill illumination for quantum efficiency measurements and subsequent spectral mismatch correction eliminates any contribution to the measured device performance from light collection from outside the device area. The low lateral conductivity of the photoactive PbS QD layer—carrier diffusion lengths

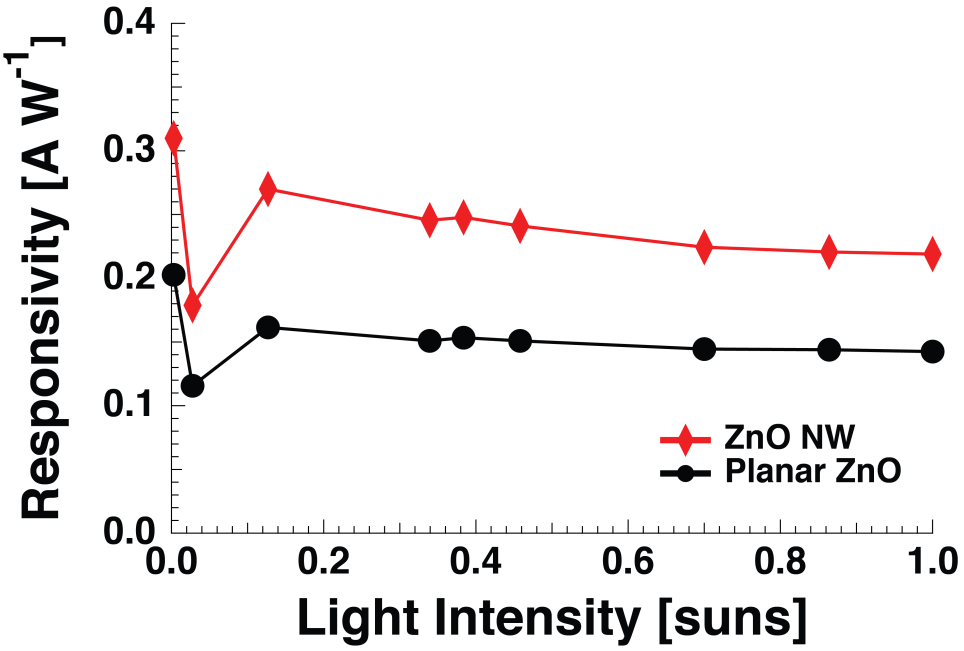

Figure 3.3: *Responsivity of planar (black circles) and nanowire-based (red diamonds) QDPV devices as a function of light intensity. The flat dependence of responsivity on light intensity justifies the measurement of EQE spectra without bias illumination.*

are on the order of 100 nm—suggests that photocurrent collection from outside the defined device area should be minimal.

■ 3.2 Light Intensity Dependence

Intensity-dependent J-V measurements show that the open-circuit voltage of nanowire devices drops off sharply at low light intensities, which suggests that trap-mediated recombination at the heterojunction interface may be enhanced due to the increased junction area (Figure 3.4). Such traps are likely saturated at high light intensities, allowing the photovoltage to approach that of planar devices (Figure 3.5). Further evidence for this interpretation can be found in the intensity-dependent series and shunt resistance trends shown in Figure 3.5. The series resistance of nanowire devices tracks that of planar devices at varying light intensity, as expected; under forward bias (where R_s is measured), the device is flooded by electrically injected carriers, and the resulting saturation of interface traps limits their effect on carrier transport. The shunt resistance, on the other hand, is much lower for nanowire devices than for planar devices at low

light intensities; the low carrier densities under reverse bias result in a higher proportion of carriers interacting with interface trap states.

The observed dependence of NW-QDPV device performance on light intensity suggests, perhaps counterintuitively, that increased junction area does not always result in improved performance in a thin-film solar cell. That said, at 1 sun illumination, the photocurrent lost to increased recombination is far outweighed by the current gained from improved carrier extraction. Achieving an optimal balance between increased recombination and enhanced carrier collection with increasing interface area may guide the further development of bottom-up-grown ordered BHJ devices.

■ 3.3 Morphological and Structural Effects on NW-QDPV Performance

Morphological and structural considerations are paramount for NW-QDPVs: Vertical nanowire alignment, inter-nanowire spacing, QD infiltration, and back-contact conformality all affect device performance. We find that visual inspection of device cross-sections can often explain the observed performance trends. In this study, we rely on focused ion beam (FIB) milling and subsequent cross-sectional electron microscopy as a primary diagnostic tool for investigating structure-related effects. Figure 2.12 shows a representative NW-QDPV device cross-section prepared by FIB milling. SEM analysis reveals individual layer thicknesses and incomplete infiltration of the QDs into the nanowire array. Inter-nanowire regions devoid of QDs appear darker in SEM images than the surrounding region. These voids potentially limit device performance by reducing both the optical thickness of the QD film and the fraction of the junction area available for charge collection.

■ 3.3.1 QD Thickness Dependence

As should be evident from Chapter 1, the thickness of the QD film is the key variable used to trade off absorption and collection in QD solar cells; this trade-off is most clearly demonstrated by the decrease in short-circuit current density for both very thin and very thick films. The effect of QD film thickness on planar and nanowire-based QDPV performance is illustrated in Figure 3.6. For the nanowire lengths used here ($\sim$200 nm), the optimal QD film thicknesses are similar for planar and nanowire-based architectures—230 nm and 240 nm, respectively. Improved performance in NW-QDPV devices thus stems primarily from enhanced charge extraction efficiency rather than increased absorption.

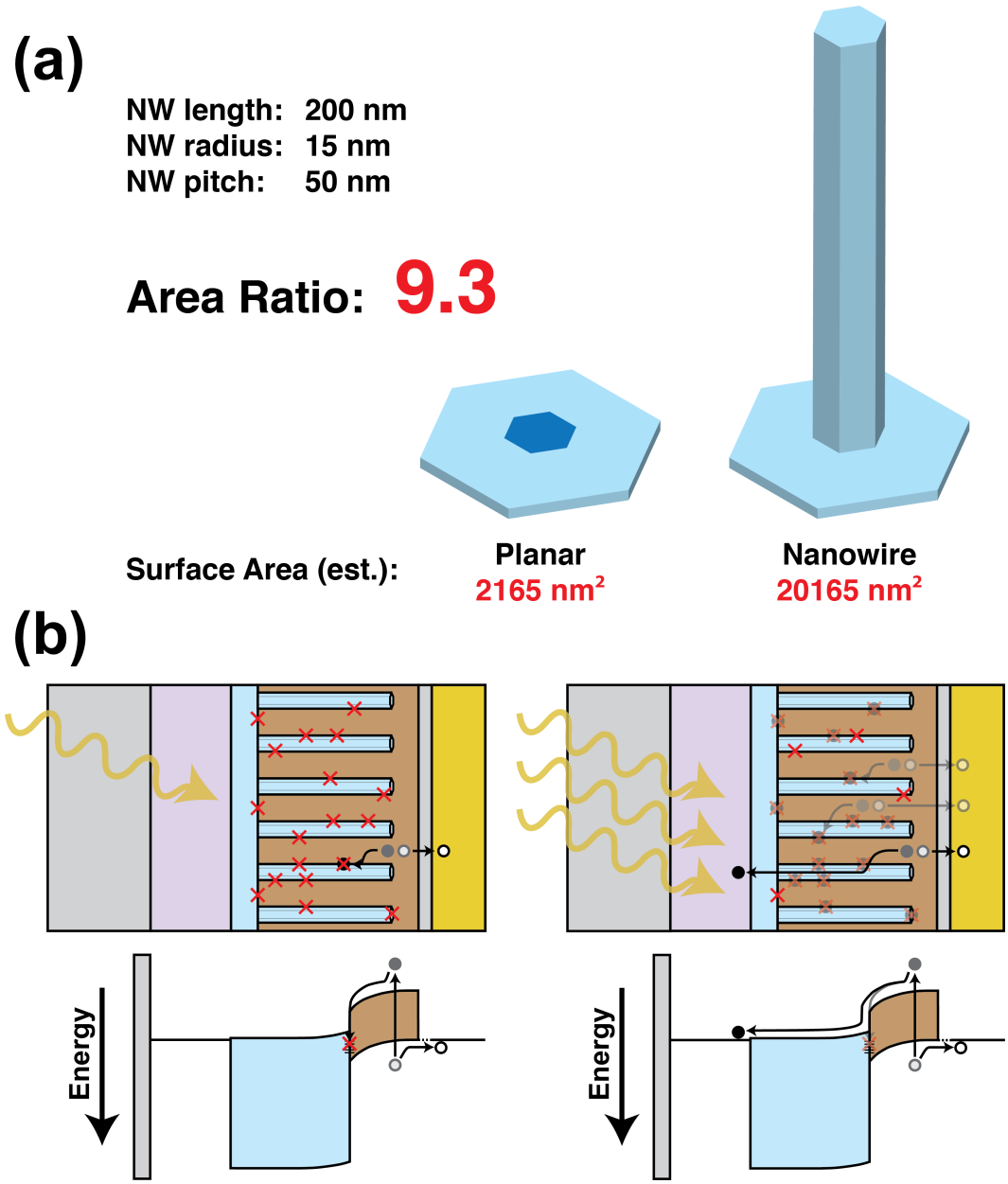

Figure 3.4: *Schematic of trap-mediated recombination process at the heterojunction interface. (a) Adding 1-D nanowires increases the total interface area in a QD solar cell by an order of magnitude. (b) At low light intensities, many of the photogenerated carriers recombine via interface traps; at high intensities, trap saturation allows photocarriers to be extracted.*

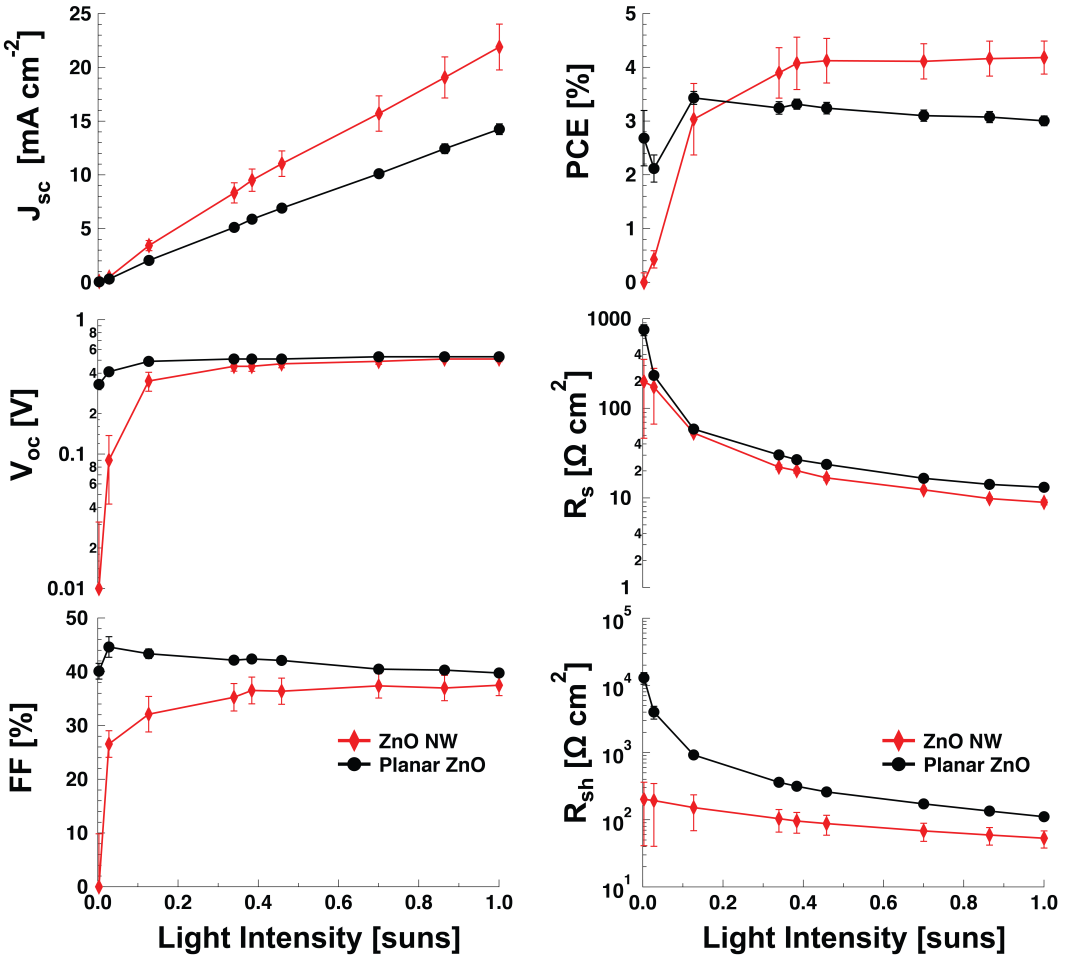

Figure 3.5: *Effect of light intensity on the performance of planar (black circles) and nanowire-based (red diamonds) QDPV devices. The intensity of AM1.5G illumination was varied using a series of neutral density filters. The open-circuit voltage of nanowire devices drops off sharply at low light intensities, which suggests that trap-mediated recombination at the heterojunction interface may be enhanced in BHJ devices due to the increased interface area. Such traps may be saturated at high light intensities, allowing generation of a photovoltage approaching that of the planar device.*

■ 3.3.2 MoO_3 Thickness Dependence

We find that the performance of NW-QDPV devices is particularly sensitive to the thickness of the MoO_3 buffer layer. Previous work has shown that a thermally-evaporated MoO_3 interlayer can enhance planar QDPV performance by eliminating the reverse Schottky barrier at the anode and protecting the QDs from damage during destructive back contact deposition[18, 46, 53]. In nanowire-based devices, MoO_3 still serves the

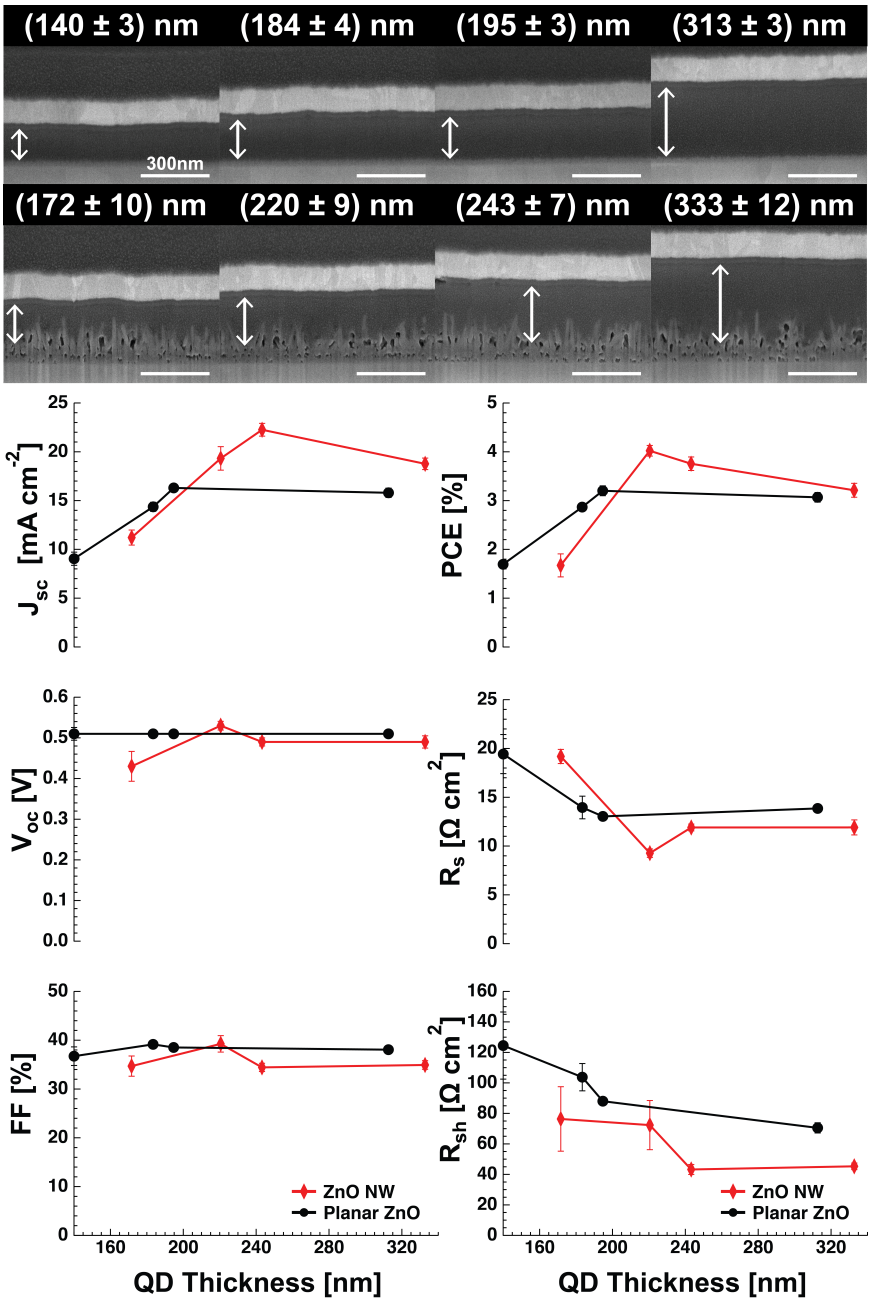

Figure 3.6: *SEM images and performance trends illustrating the effect of PbS QD film thickness on planar (black circles) and nanowire-based (red diamonds) QDPVs. The power conversion efficiency (PCE) peaks between 200 nm and 240 nm for both planar and nanowire devices (with nanowires of length ∼200 nm), which suggests that the increased short-circuit current density (J_{SC}) and PCE of nanowire devices stems primarily from improved charge extraction rather than enhanced light absorption. Data from other device runs (not shown) indicate that planar device efficiencies remain roughly constant at ∼3% for QD film thicknesses of 200-240 nm.*

same electronic purpose, but more importantly, it also acts as a physical buffer against shorting. As mentioned above, non-uniformity in nanowire length forces a compromise between series and shunt resistance losses. To avert direct shorting, the QD film must be thick enough to cover even the longest nanowires. In regions with shorter nanowires, however, part of the QD film remains undepleted, and electrons and holes must traverse a wide quasi-neutral region, suffering increased recombination losses along the way. A thick MoO_3 layer can decouple shorting problems from series resistance losses—the QD film thickness can then be tailored to the average nanowire length, since unusually long nanowires left partly uncovered can contact or even penetrate the MoO_3 without shorting the device.

Figure 3.7 illustrates the effect of MoO_3 thickness on the performance of QDPV devices with and without ZnO nanowires. In both cases, the short-circuit current density, open-circuit voltage, and fill factor all increase with increasing MoO_3 thickness, up to the optimum thickness of 25 nm. Further increases in film thickness reduce the carrier collection efficiency and hence the measured photocurrent. A comparison of the forward-bias behavior of planar and nanowire-based devices in the dark (Figure 3.8) confirms the dual benefit of MoO_3: In planar devices, shunting is not an issue, and weakening of the Schottky barrier causes the dark current to increase with increasing MoO_3 thickness until resistive losses become significant. In nanowire-based devices, however, severe shunting in the absence of MoO_3 yields ohmic behavior and high currents, and the dominant role of MoO_3 as a physical buffer causes the dark current to decrease with increasing MoO_3 thickness. AFM analysis of devices with 0 nm and 25 nm MoO_3 (Figure 3.9) suggests that Au deposited on top of MoO_3 conforms more readily to exposed nanowire tips than Au alone, reducing direct ZnO-to-Au shunting and potentially enhancing absorption by scattering incoming light and increasing the optical path length through the active layer.

The profound impact of MoO_3 thickness on NW-QDPV device performance points to a general design strategy for nanostructured photovoltaics, for which shorting remains a major problem due to the intentional introduction of local non-uniformities in film thickness. A properly chosen buffer layer like MoO_3 can mitigate shorting without hindering charge extraction.

In the next chapter, we take a step back and consider the effect of material choices on the viability of nanostructured QDPVs for future solar applications. In particular, we now explore the possibility of using graphene as a transparent conductive electrode to replace ITO in thin-film solar cells.

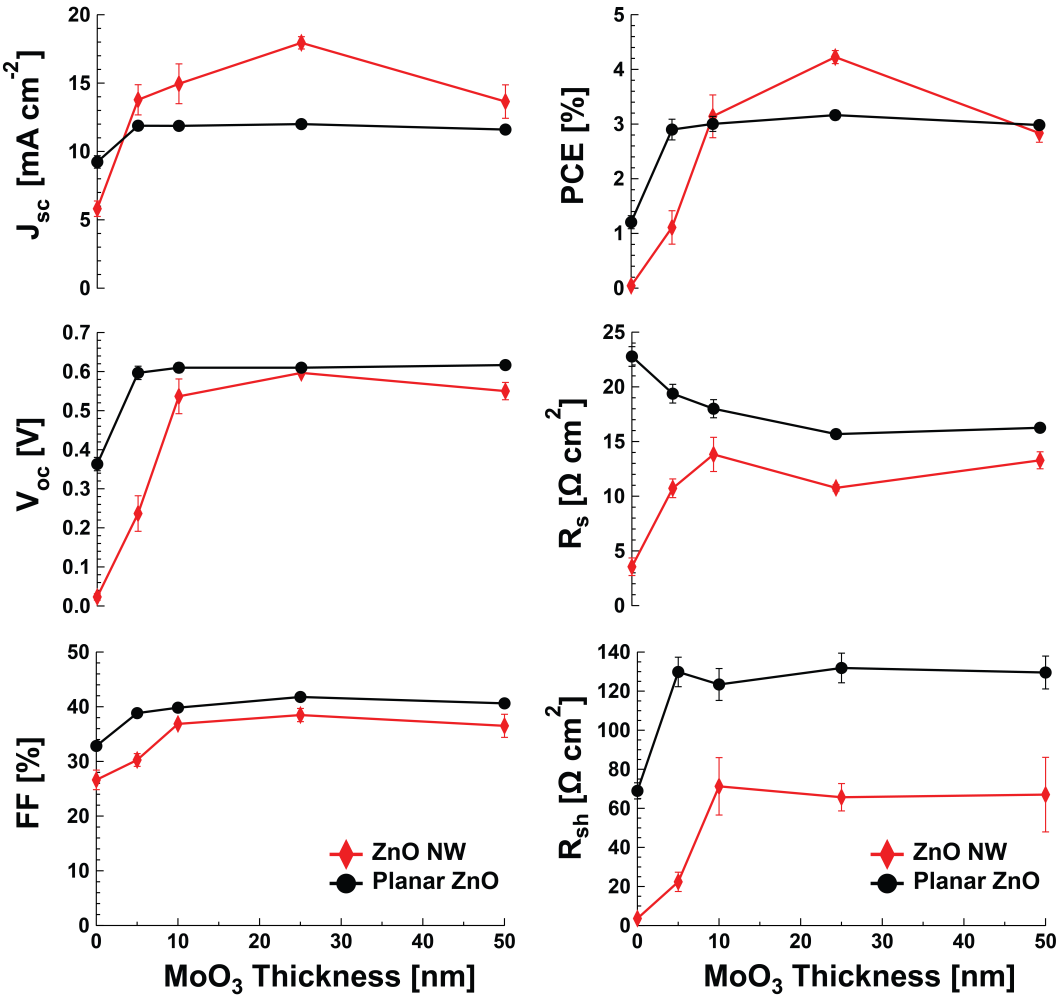

Figure 3.7: *Effect of MoO_3 thickness on planar (black circles) and nanowire-based (red diamonds) QDPV device performance. Increasing MoO_3 thickness—up to the optimum value of 25 nm—enhances the short-circuit current density (J_{SC}), open-circuit voltage (V_{OC}), fill factor (FF), and power conversion efficiency (PCE) of both planar and nanowire devices. Nanowire-based devices are significantly more sensitive than planar devices, with a sharp drop-off in performance with either too thin or too thick of a MoO_3 layer.*

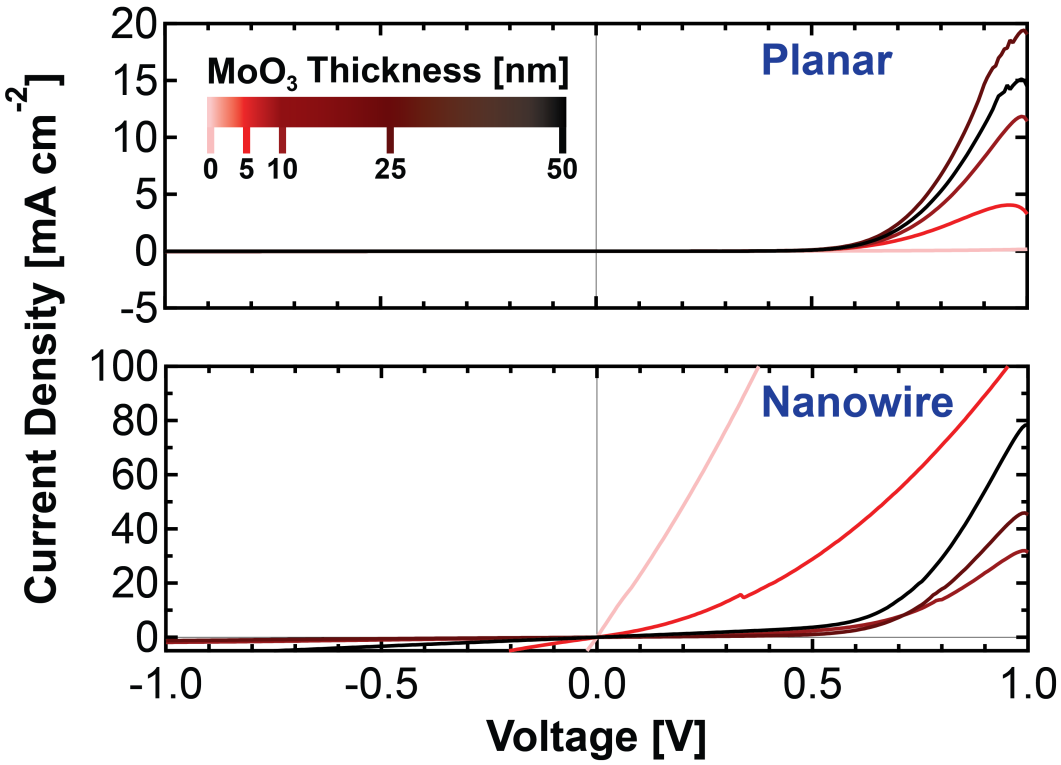

Figure 3.8: *Dark J-V characteristics showing effect of MoO_3 thickness on planar (top) and nanowire-based (bottom) QDPV devices. A MoO_3 interlayer eliminates the anode Schottky barrier and improves all PV performance parameters. For nanowire-based devices, MoO_3 also provides a physical buffer against shorting between the ZnO nanowires and the Au electrode. At a given voltage, planar devices exhibit an increase in dark current density with increasing MoO_3 thickness (up to 25 nm), reflecting an increase in conductance due to reduction of the Schottky barrier. Nanowire devices instead exhibit a decrease in dark current with increasing MoO_3 thickness, reflecting a decrease in conductance due to elimination of shunts.*

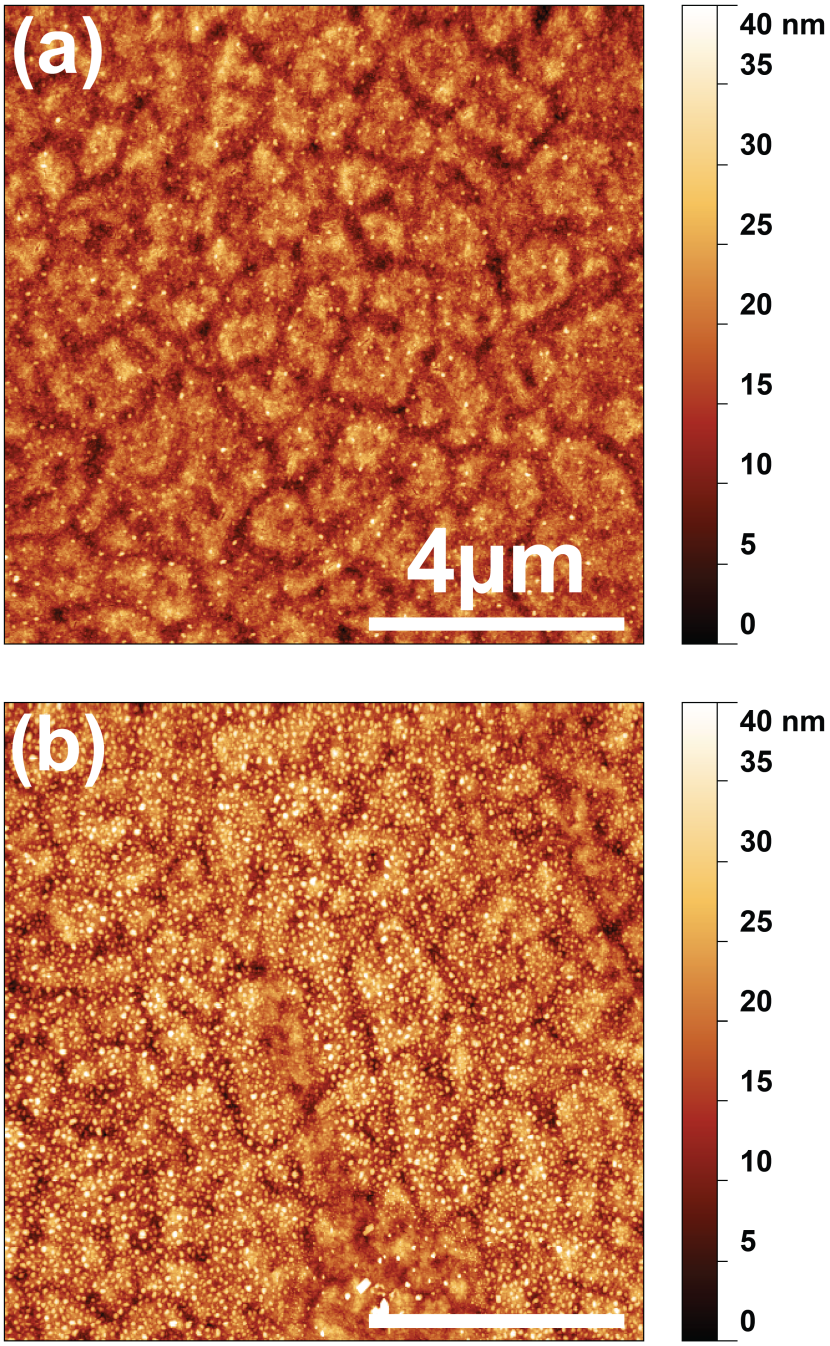

Figure 3.9: *AFM images of the Au electrode on nanowire-based QDPV devices with (a) 0 nm or (b) 25 nm of MoO_3 between PbS QDs and Au. The MoO_3 buffer layer may help the electrode conform to protruding ZnO nanowires, thus reducing the probability of shorting. The RMS surface roughness of the Au contact is 4.4 nm without MoO_3 and 6.1 nm with 25 nm MoO_3.*

Chapter 4

Graphene Electrodes for Nanostructured QDPVs

AMONG the key motivations for using bottom-up nanostructures and colloidal QDs for solar photovoltaics are the abundance of the constituent materials and the prospect of low-temperature device fabrication. The solar cells described in this thesis could be fabricated cheaply on lightweight, flexible substrates—e.g., ultra-thin glass, thermoplastics, or paper—which could in turn enable novel PV applications at vastly reduced cost and unprecedented specific power per weight, measured in W g^{-1}.

To maintain these advantages at scale, however, we cannot continue to rely on transparent electrodes based on tin-doped indium oxide (ITO). ITO boasts both high electrical conductivity ($\sim 1 \times 10^3$ S cm^{-1}) and high optical transparency (over $\sim$70%) for wavelengths above $\sim$400 nm[54], and most modern thin-film solar cells are fabricated on rigid glass substrates sputter-coated with ITO. But indium is a rare metal produced as a byproduct of the mining and refining of major metals—primarily Zn ores—with much higher production volumes and established markets[55]. The resultant high cost and market volatility may disqualify ITO for utility-scale solar harvesting, where the primary system performance metrics are based on cost—either cost per unit power (in units of USD W^{-1}) or levelized cost of energy (LCOE) over the system lifetime (USD kWh^{-1}). Furthermore, the brittleness of thin ITO films[56] limits their use in flexible optoelectronic devices. To realize a flexible and scalable thin-film solar cell, we must therefore find an alternative transparent conductive electrode material that is both abundant and mechanically robust.

■ 4.1 Introduction to Graphene

Graphene is a carbon monolayer with a planar hexagonal lattice structure and semimetallic electronic behavior. It was isolated for the first time in 2004 by Geim and Novoselov[57, 58, 59] and has since sparked extensive research efforts on a wide assortment of applications in logic, chemical sensing, and energy conversion and storage[60]. Graphene exhibits superior carrier transport properties, unmatched mechanical strength, and high optical transparency at all wavelengths, and could thus serve as a transparent, flexible electrode for solar cells and light-emitting devices[60].

Combining the properties of graphene and semiconducting nanowires would provide a unique platform for the development of nanostructured solar cells with superior transparency, flexibility, and photovoltaic performance. But growing nanostructures directly on pristine graphene without impairing its electrical and mechanical properties has been challenging due to graphene's stable and inert sp^2-hybridized structure. High temperature ($\sim$400 °C) metal-organic vapor phase epitaxy (MOVPE) growth of ZnO nanowires on graphene has been demonstrated[61], but this process requires destructive oxygen plasma treatment of the graphene substrate to generate step edges that act as nanowire nucleation sites. While the simple hydrothermal growth method has been suggested[62], no optoelectronic devices have yet been demonstrated using hydrothermally grown ZnO nanowires and graphene, thus leaving an open question about the structural and electrical integrity of the graphene during the nanowire growth process.

Here we show that graphene can be integrated with ZnO nanowires to form the transparent cathode in a fully nanostructured colloidal quantum dot solar cell, shown in Figure 4.1. We grow ZnO nanowires on graphene, fabricate ordered bulk heterojunction QDPVs, and demonstrate prototype devices with photovoltaic performance approaching that of ITO-based solar cells. This is the first demonstration of an optoelectronic device based on hydrothermally grown ZnO nanowires on graphene, and preliminary results suggest that graphene could serve as a viable replacement for ITO in future optoelectronic device applications.

■ 4.2 Fabrication of Graphene-Based QD Solar Cells

Co-authorship note: Parts of the following two sections are derived from a recent collaborative work[45]. Experiments on graphene synthesis and ZnO nanowire growth on graphene were primarily carried out by Hyesung Park and Sehoon Chang.

In this study, ZnO nanowires are grown on both graphene and ITO electrodes, and

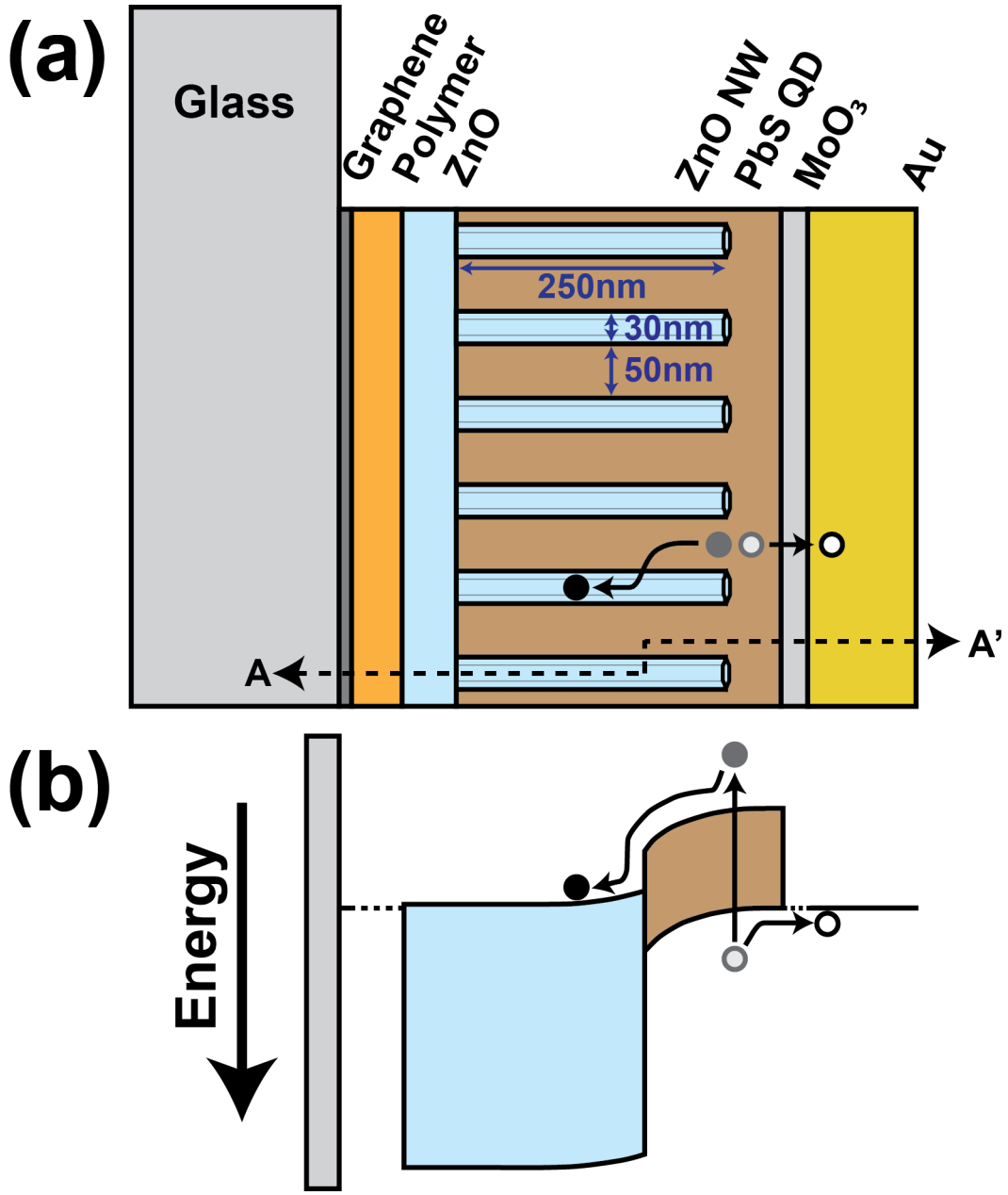

Figure 4.1: *Graphene-based NW-QDPV architecture. (a) Schematic and (b) energy band diagram (cross-section along A-A') of an ordered bulk heterojunction QDPV with a trilayer graphene cathode. Modification of the graphene surface with a polymer interlayer facilitates the formation of smooth, uniform ZnO seed layers and the subsequent growth of well-ordered ZnO nanowire arrays.*

both architectures are used for subsequent device fabrication and testing. Fabrication of ordered BHJ QDPV devices on graphene involves the following processing steps:

1. Low-pressure CVD growth and transfer of graphene
2. Deposition of interfacial polymer layer
3. Sol-gel deposition of ZnO seed layer
4. Hydrothermal growth of ZnO nanowires
5. Spin-casting of PbS quantum dots
6. Thermal evaporation of MoO_3 and Au

We focus here on steps 1 and 2, the detailed preparation of the graphene cathode—the remaining steps are identical for graphene- and ITO-based devices and are described in Chapter 2.

■ 4.2.1 Graphene Synthesis

Monolayer graphene films are synthesized by low-pressure chemical vapor deposition (LPCVD) using 25 μm thick copper foil as a metal catalyst[45, 63, 64]. At a base pressure of 30-50 mTorr, the growth chamber is first heated to 1000 °C under hydrogen gas (H_2, 10 sccm, ∼320 mTorr) for 30 minutes; methane gas (CH_4, 20 sccm, ∼810 mTorr total) is then introduced for a growth period of 30 minutes. Following growth, the chamber is cooled to room temperature at a rate of ∼45 °C min^{-1}.

To transfer graphene from Cu foil to a glass substrate for subsequent device fabrication, a poly(methyl methacrylate) (PMMA) support layer is used[64]. PMMA is first spin-cast on the graphene surface, and graphene on the backside of the Cu foil is removed by reactive ion etching (RIE) with oxygen gas at 100 W and a base pressure of 7×10^{-5} Torr. The foil is then etched away with Cu etchant, graphene films are thoroughly rinsed with 10% hydrochloric acid and DI water, and the PMMA is removed by annealing at 500 °C for 2 hours under H_2 and Ar gas at flow rates of 700 sccm and 400 sccm, respectively. The transfer process is repeated twice to form stacked three-layer graphene films on glass substrates, with average sheet resistance and transmittance values of $300 \pm 12\ \Omega\ \square^{-1}$ and $(92.0 \pm 0.4)\%$, respectively, similar to those reported elsewhere[65].

■ 4.2.2 Interfacial Modification using a Polymer Interlayer

A critical step in the hydrothermal growth of ZnO nanowires is the deposition of a uniform, high-quality ZnO seed layer. The simple sol-gel process described earlier yields a uniform ZnO film on ITO, but graphene's low surface free energy[66] and hydrophobic nature[67] result in poor wetting by the polar sol-gel solution, which forms dewetted ZnO islands on the graphene surface (Figure 4.2). Similar dewetting effects on graphene have been reported with other material systems, including poly(3,4-ethylenedioxythiophene):poly(styrenesulfonate) (PEDOT:PSS), a transparent conductive polymer commonly used as a hole injection layer in organic optoelectronic devices. It would thus be desirable to identify a nondestructive method for modifying the graphene surface to enable uniform deposition of a ZnO seed layer.

In this work, we modify the graphene surface with conducting polymers that (1) wet the graphene surface, (2) provide a more chemically compatible surface with ZnO, and (3) enable charge transfer between the ZnO and the graphene. Two commercially available conducting polymers are used: (1) poly(3,4-ethylenedioxythiophene)-block-poly(ethylene glycol) doped with perchlorate (PEDOT:PEG(PC)), and (2) sulfonated poly(thiophene-3-[2-(2-methoxyethoxy)-ethoxy]-2,5-diyl) (RG-1200). The polymers are dissolved in solvents with good wetting properties on graphene (nitromethane and ethylene glycol monobutyl ether/water, respectively) and spin-cast on graphene films in ambient atmosphere[45]. We find that surface modification of graphene with either polymer yields uniform ZnO films, as determined by visual inspection and AFM characterization (Figures 4.2 and 4.3).

ZnO nanowire arrays are grown on ITO and modified graphene substrates by the standard hydrothermal procedure described in Chapter 2. Notably, the morphology of nanowires grown on the modified graphene substrates is similar to that obtained on ITO (Figure 4.4). ZnO nanowire arrays grown on a graphene/RG-1200 substrate exhibit better alignment than those on graphene/PEDOT:PEG(PC) and comparable alignment to arrays grown on ITO.

The above results demonstrate the broad applicability of our proposed approach for growing well-ordered ZnO nanowires on a graphene surface via nondestructive modification with conductive polymeric interlayers. To elucidate possible electronic interactions—e.g., doping via charge transfer—between graphene, the polymer interlayer (PEDOT:PEG(PC)), and the ZnO seed layer, we perform resonant Raman spectroscopy analysis, a fast and nondestructive technique that has been used extensively to study structural changes and the effect of doping in polymers and in graphene[68, 69, 70].

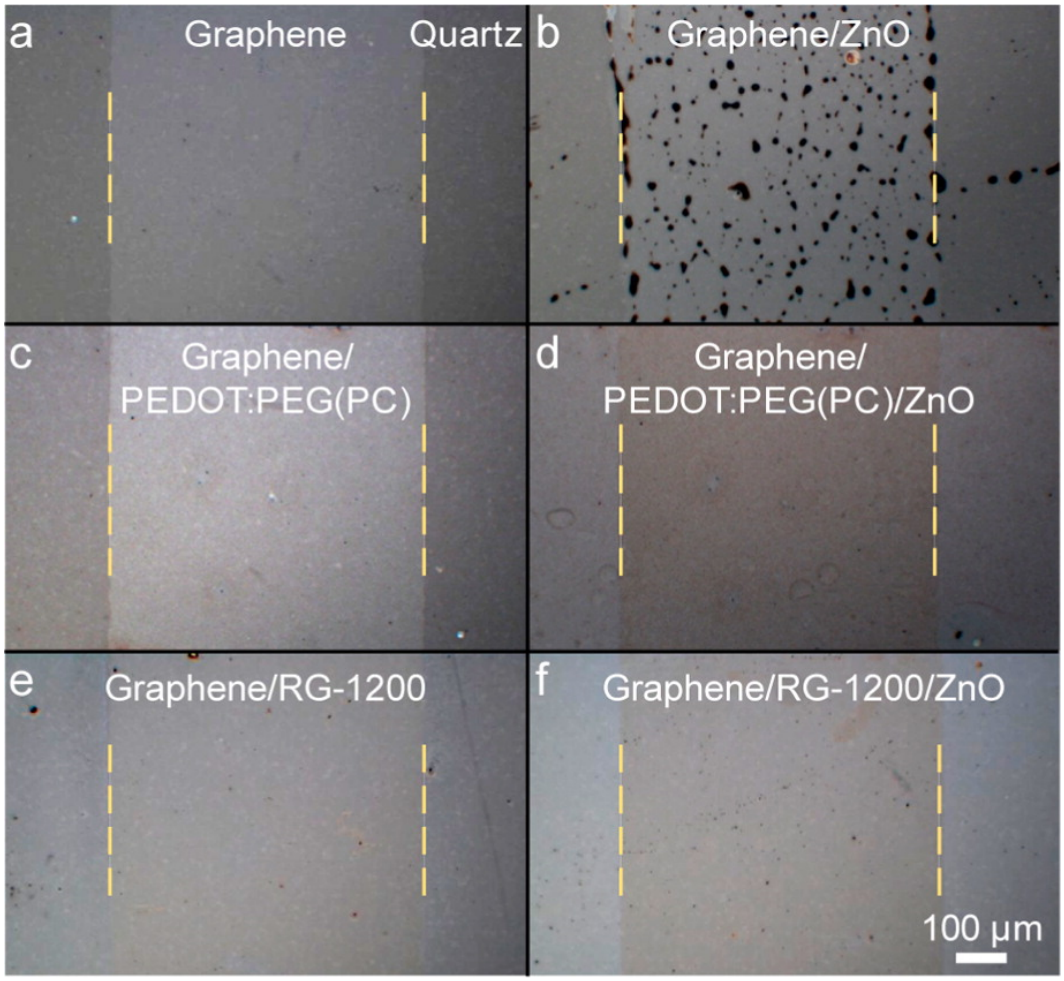

Figure 4.2: *ZnO seed layer wetting properties on polymer-modified graphene substrates. Bright-field optical microscopy images of (a) graphene on a quartz substrate, (b) ZnO spin-coated on pristine graphene, showing ZnO dewetting and island formation, (c, d) graphene/PEDOT:PEG(PC) before and after ZnO deposition, and (e, f) graphene/RG-1200 before and after ZnO deposition. Parts (c)-(f) illustrate the uniform coverage of both polymers on the graphene surface and of the ZnO seed layer on the polymer-modified graphene.*

The results are summarized in Figure 4.5: The characteristic carbon-carbon (C=C) stretch vibration in the PEDOT:PEG(PC) Raman spectrum (at 1441 cm^{-1}) red-shifts upon contact with ZnO and blue-shifts upon contact with graphene, corresponding to reduction of the polymer by ZnO and oxidation by graphene. From these observations, we expect electrons to transfer from ZnO to the conducting polymer PEDOT:PEG(PC) and ultimately to the graphene electrodes, as desired in a full device configuration.

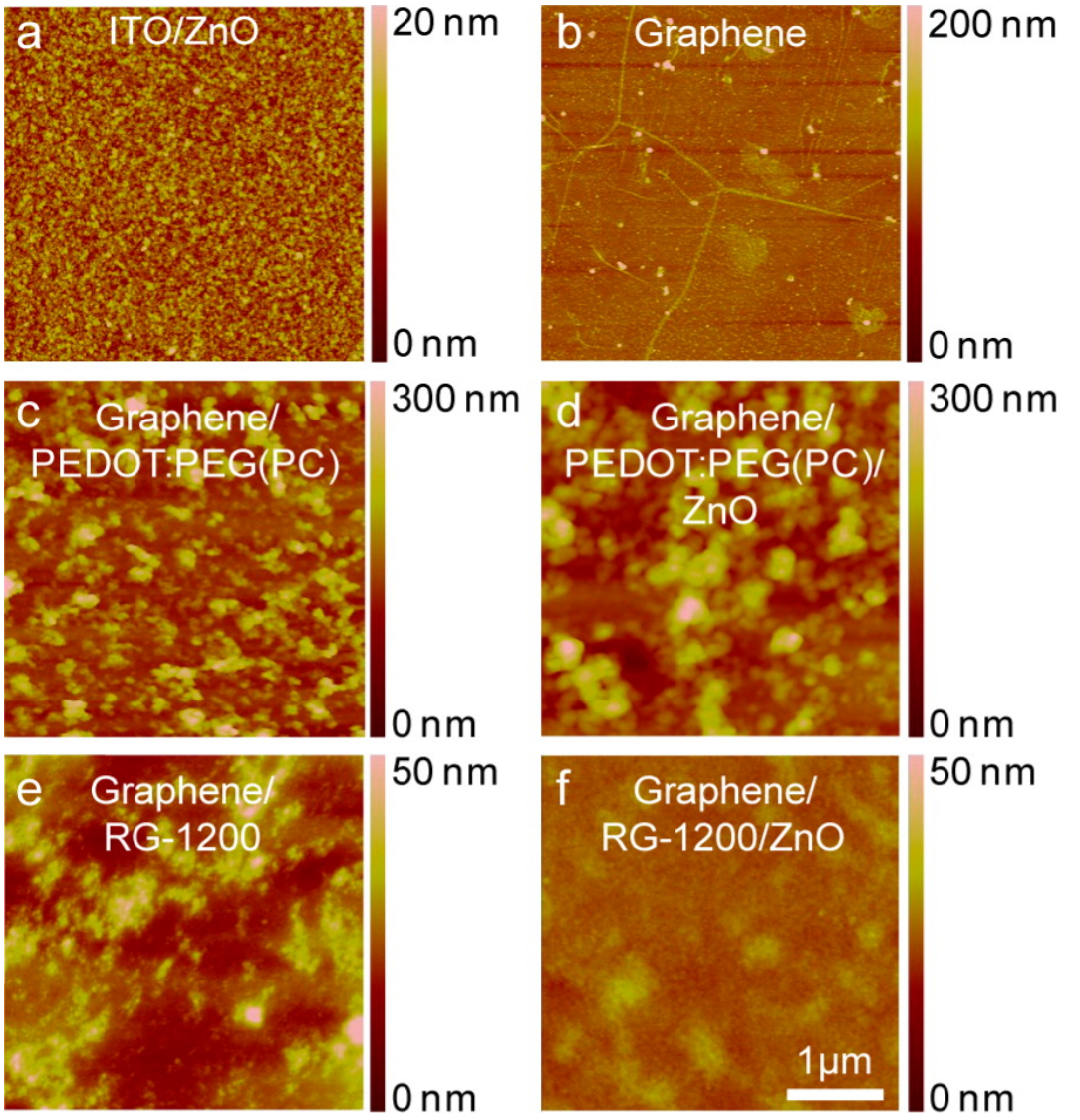

Figure 4.3: *Surface morphology analysis of ZnO seed layers on various substrates. Tapping-mode AFM images of (a) ZnO on ITO, (b) bare graphene, (c, d) PEDOT:PEG(PC) on graphene before and after ZnO seed layer deposition, and (e, f) RG-1200 on graphene before and after ZnO deposition. Both polymers completely coat the graphene surface, as seen in (c) and (e), and sol-gel ZnO in turn conformally covers the underlying polymers, as seen in (d) and (f). The polymer surfaces are smoothed by the ZnO overlayer: RMS surface roughness is reduced from 34 nm to 25 nm for PEDOT:PEG(PC) and from 6 nm to 2 nm for RG-1200.*

After ZnO nanowire growth, we complete the fabrication of graphene-cathode ordered BHJ QD solar cells by following the procedure outlined in Chapter 2: We spin-cast QDs, then thermally evaporate MoO_3 and Au. The full device structure and corresponding

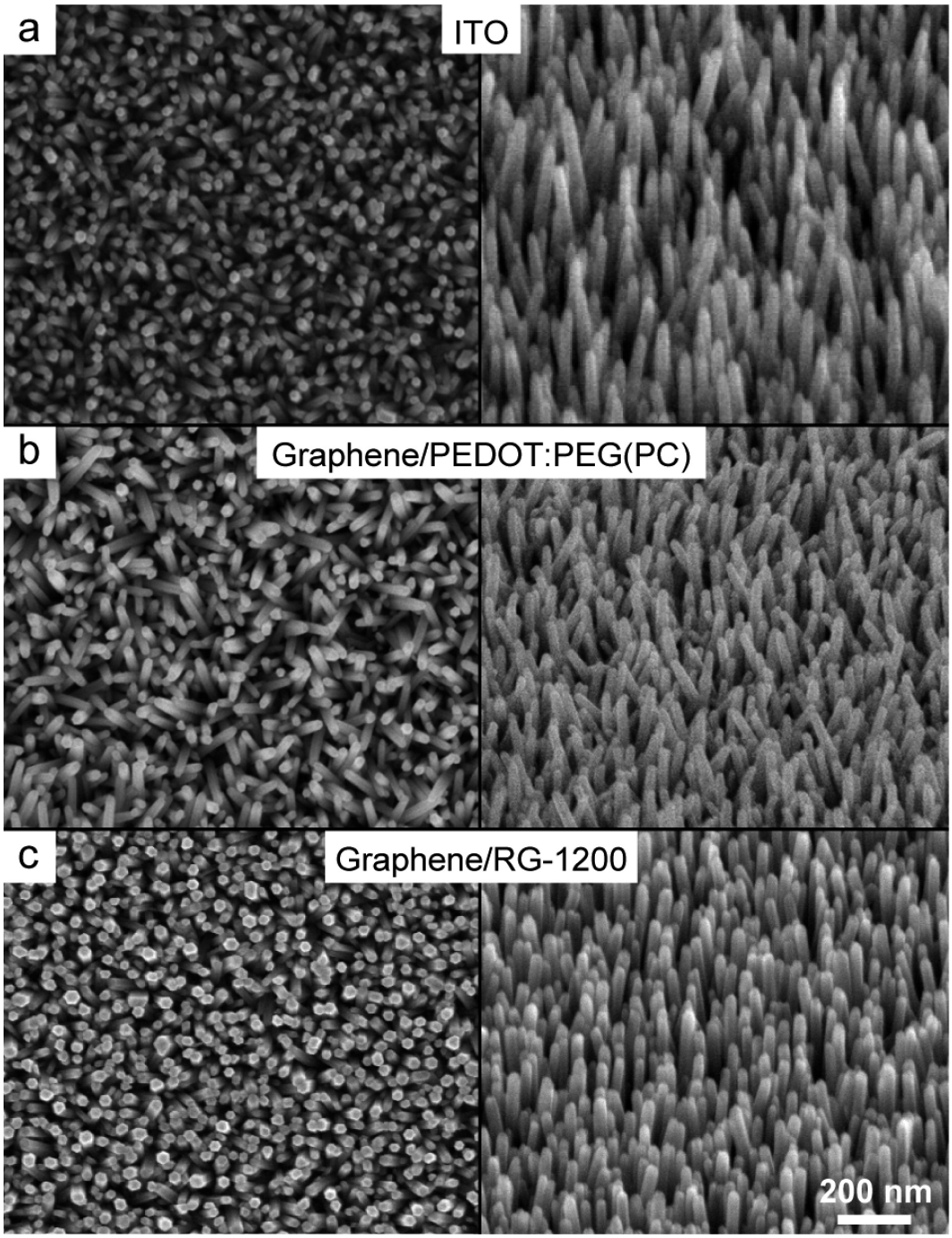

Figure 4.4: *SEM characterization of ZnO nanowire arrays grown on ITO and on polymer-modified graphene. Nanowire arrays grown under identical experimental conditions on (a) ITO, (b) graphene/PEDOT:PEG(PC), and (c) graphene/RG-1200 exhibit similar areal densities, and the graphene/RG-1200 combination yields uniformity and alignment comparable to that of ITO.*

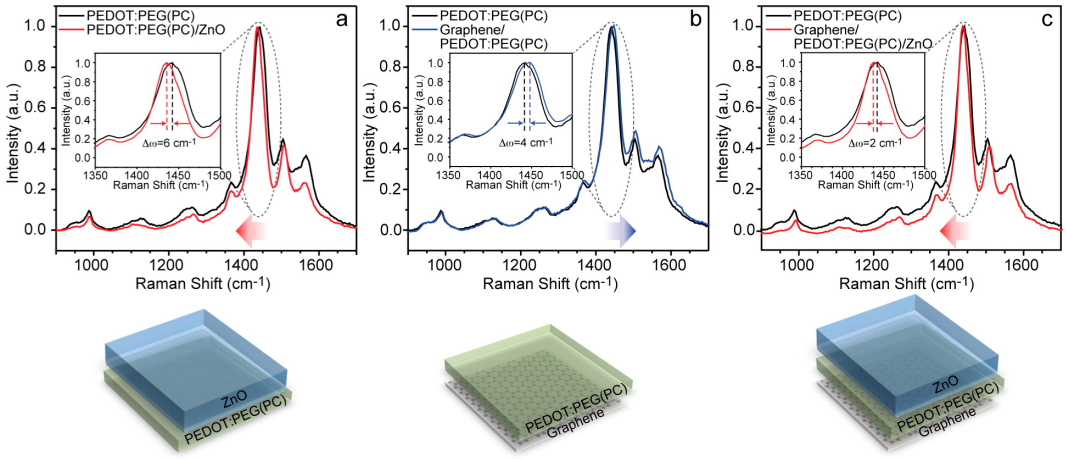

Figure 4.5: *Raman analysis of PEDOT:PEG(PC) and its hybrid counterparts. (a) Raman spectra of PEDOT:PEG(PC) with and without ZnO, with peak P1 centered at 1441 cm^{-1}. The polymer is reduced upon interaction with ZnO, as evidenced by a decrease in frequency (red-shift by 6 cm^{-1}) at 1441 cm^{-1}. (b) Peak P1 is blue-shifted by 4 cm^{-1} when the PEDOT:PEG(PC) is in contact with graphene. (c) Peak P1 exhibits a net red-shift by 2 cm^{-1} in the full graphene/PEDOT:PEG(PC)/ZnO system. In all of these plots, the intensities are normalized to their maximum values to facilitate comparison of spectral features.*

band diagram are shown in Figure 4.1.

■ 4.3 Performance Comparison with Conventional ITO-Based Devices

J-V characteristics of nanowire-based QD solar cells with graphene and ITO cathodes are shown in Figure 4.6, with cross-sectional SEM images inset. Graphene-based devices with either polymeric interfacial layer achieve performance comparable to that of ITO control devices, with average power conversion efficiencies of $(3.3 \pm 0.6)\%$, $(3.8 \pm 0.3)\%$, and $(4.4 \pm 0.6)\%$ for graphene/RG-1200, graphene/PEDOT:PEG(PC), and ITO cathode devices, respectively.

Our work constitutes the first demonstration of a graphene-based photovoltaic device employing hydrothermally-grown ZnO nanowires[45]. This demonstration hinges on a simple interfacial polymer treatment that facilitates conformal, smooth wetting of the ZnO seed layer and subsequent ordered nanowire growth. With graphene electrodes consisting of only three stacked monolayers, photovoltaic performance approaches that of ITO-based solar cells in preliminary tests. These results indicate that the proposed method for polymeric interfacial modification enables the growth of high-quality ZnO nanowire arrays on graphene while preserving its electrical and structural properties.

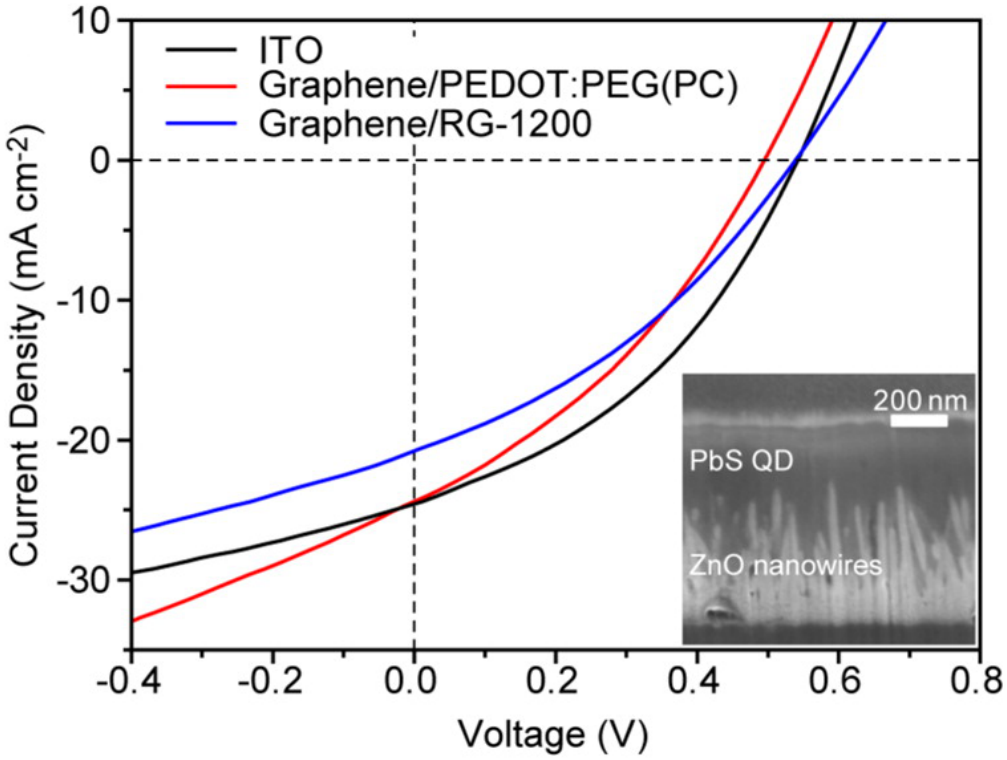

Figure 4.6: *Performance of graphene-based ordered bulk heterojunction QD solar cells. J-V characteristics under AM1.5G illumination of champion devices with different polymer interlayers. Graphene-cathode NW-QDPVs with PEDOT:PEG(PC) (red) and RG-1200 (blue) interlayers perform similarly to a control device on ITO (black). Inset is a cross-sectional SEM image of the complete device, showing substantial infiltration of the QDs into the nanometer-scale gaps between ZnO nanowires.*

In contrast to physical etching, this substrate-independent approach allows for non-destructive processing of graphene-based devices, and the results suggest that graphene could serve as a viable alternative to ITO in thin-film photovoltaic applications.

Chapter 5

Future Directions for Quantum Dot Solar Cells

THE computational modeling community uses the term "multiscale" to describe strategies for simulating physical systems with important features on multiple physical length scales. Although the present work is primarily experimental, multiscale thinking can provide valuable direction for the field of quantum dot photovoltaics (Figure 5.1). We can classify important areas of investigation under various length scales, from individual QDs to assemblies to films to complete devices. Understanding derived from studies on one length scale can motivate experimental design and clarify experimental findings on other length scales. For example, on the scale of individual QDs, we investigate synthetic approaches to controlling QD size, shape, stoichiometry, and doping, guided by the demands of an efficient solar cell: monodisperse sizes, stoichiometric surfaces, and low doping concentrations. The intimate knowledge of QD surface chemistry derived from synthetic experience in turn drives the analysis of electronic trap states and QD-ligand interactions in QD assemblies. The resulting interface dipoles dictate Fermi levels and carrier transport behavior in QD films. With material and transport parameters in hand, we can select complementary contact and interlayer materials to minimize interfacial energy barriers, then design a device architecture to overcome the fundamental transport limitations inherent in disordered semiconductors.

Despite their wide-ranging spatial extent, most of the above physical phenomena can be studied using similar experimental techniques—primarily film- and device-level characterization. It is on these length scales that the device engineer can contribute most, and in so doing, make major strides toward a more efficient QD solar cell.

We need reliable techniques for characterizing the electronic properties of QD films, particularly accurate methods for extracting the transport parameters so beloved by

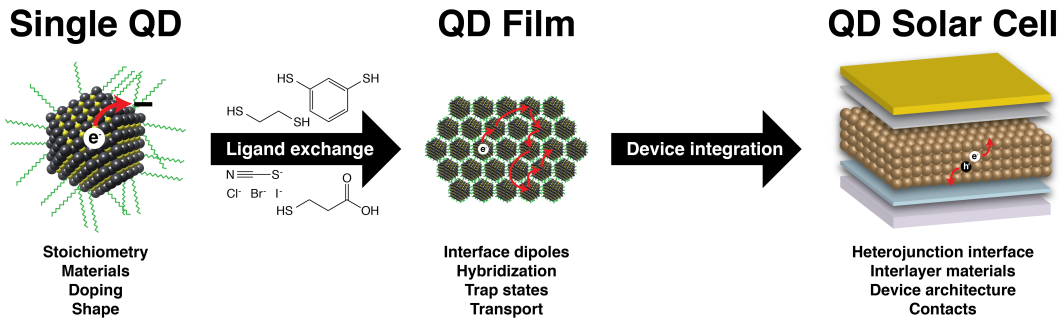

Figure 5.1: *Multiscale paradigm for experimental QDPV research. At each length scale from individual QDs to QD films to QDPV devices, unique physical phenomena govern electronic behavior. Advances in understanding derived from computational and experimental investigations at any scale can clarify findings and guide design at other length scales.*

device engineers—majority carrier types, mobilities, depletion widths, and diffusion lengths. These parameters are often measured today using the ubiquitous field-effect transistor (FET) structure. But to translate a conventional device architecture to highly unconventional semiconductors requires a solid physical and theoretical basis that is currently lacking in the scientific literature. Comparing QD-FETs and conventional MOSFETs, we observe several important structural and phenomenological differences: Schottky source/drain contacts, a fully depleted and floating body, hopping transport, and strong bias-stress transients, to name just a few. Yet many literature reports on QD-FETs simply apply conventional MOSFET theory, with neither refinement nor rationale. A tight integration of computational studies (e.g., atomistic modeling of the effect of ligands on doping in QD films) and experimental investigations may well inform the realization of custom-tailored QD films, and eventually both elucidate the QD-FET operating mechanism and determine what can and what cannot be reasonably deduced from field-effect measurements on QD films.

Further performance gains in quantum dot photovoltaics may be realized through device-scale computational modeling of the effects of the size, morphology, and density of 1-D nanostructure arrays on carrier collection efficiency. The performance enhancements demonstrated in this work stem primarily from improved charge extraction efficiency; longer nanowires and thicker active films will be necessary to increase the fraction of light absorbed. While we can grow longer nanowires by simply increasing the growth time, their average diameter also increases with time. Since the density of nucleation sites is fixed, the spacing between nanowires decreases with growth time, hindering

QD infiltration. Furthermore, the absolute variance in nanowire lengths in a bottom-up-grown array increases with the average length, confounding optimization efforts and exacerbating shorting issues. Reaching the ultimate goal of micron-long nanowires and thick, fully-depleted, void-free QD films will thus require improved strategies for infiltrating QDs into nanowire arrays, including nanowire density control, interface modifications, and novel QD deposition techniques.

Combining novel film treatments—as characterized by accurate charge transport measurements—with nanostructured device architectures may ultimately produce high-performance QD solar cells. Advances in synthetic processes could provide a consistent QD platform for higher-level investigations, while optimized computational models can span the parameter space more efficiently than experimentation alone. Furthermore, with the physical insight derived from extensive film- and device-scale studies, we may hope eventually to construct a coherent model for QDPV operation using language that bridges between the two primary photovoltaic research communities: those working on inorganic depletion-mode PVs—i.e., Si, GaAs, and thin-film solar cells—and those working on excitonic PVs—i.e., small-molecule, polymer, and dye-sensitized (Grätzel) cells. Unification of the underlying physical theory and vocabulary would make QDPV research accessible to the broader scientific community and help drive the development of future PV technologies.

Even if QDPVs ultimately fail to fulfill their promise as a major source of renewable energy, quantum dots are the logical next domain for nanotechnology research. They are building blocks, the artificial atoms with which we can construct, control, and engineer our world at the nanoscale. Any research dedicated to their synthesis, science, and deployment thus will not be wasted.

Chapter 6

Conclusion

In this thesis, we demonstrated the use of hydrothermally-grown ZnO nanowires in ordered bulk heterojunction PbS colloidal quantum dot solar cells. We have proposed general criteria for the independent optimization of bottom-up 1-D nanostructures for QDPV applications, with particular emphasis on the importance of uniformity in length, diameter, and density. Through device studies and microscopic analysis, we demonstrated and explained the increased sensitivity of nanowire-based devices to light intensity and to the thickness of the MoO_3 anode buffer layer. Our NW-QDPV devices regularly achieve photocurrents of over 20 mA cm^{-2} and efficiencies of up to 4.3%, with a champion cell efficiency of 4.9%, among the highest ever reported for this material system. Furthermore, we showed that graphene can serve as a transparent conductive electrode to replace ITO in nanostructured solar cells—in particular, that vertically ordered ZnO nanowire arrays can be grown hydrothermally on graphene to produce an efficient ordered bulk heterojunction QDPV device. Together these results suggest that nanostructured device architectures can help overcome the absorption-collection trade-off in colloidal quantum dot solar cells and bring us one step closer to a fully renewable energy future. The world awaits.

Appendix A

List of Materials

All standard solvents were purchased from Sigma-Aldrich and used as received.

A.1 PbS QD Synthesis and Solar Cell Fabrication

- Patterned ITO/glass substrates (150 nm, 20 Ω $\square^{-1}$, Thin Film Devices)
- Lead acetate trihydrate (99.999%, Sigma-Aldrich)
- Hexamethyldisilathiane (Bis(trimethylsilyl) sulfide (TMS-S), synthesis grade, Sigma-Aldrich)
- Oleic acid (OLA, 90%, Sigma-Aldrich)
- 1-Octadecene (ODE, 90%, Sigma-Aldrich)
- Octane (99+%, anhydrous, Sigma-Aldrich)
- 1,3-Benzenedithiol (BDT, 99%, Sigma-Aldrich)
- Acetonitrile (99.8%, anhydrous, Sigma-Aldrich)
- MoO_3 powder (99.9995%, Alfa Aesar)
- Au pellets (99.999%, Lesker)

A.2 Sol-gel ZnO Seed Layer Deposition

- Zinc acetate dihydrate (99.999%, trace metals basis, Sigma-Aldrich)
- Ethanolamine (99.5+%, redistilled, Sigma-Aldrich)
- 2-Methoxyethanol (99.8%, anhydrous, Sigma-Aldrich)

A.3 ZnO Nanowire Growth

- Zinc nitrate hexahydrate (98%, reagent grade, Sigma-Aldrich)
- Hexamethylenetetramine (HMTA, 99+%, ACS reagent, Sigma-Aldrich)
- Deionized (DI) water

A.4 Graphene Synthesis and Surface Modification

- Copper foil (25 μm thick, Alfa Aesar)
- Poly(methyl metharylate) (PMMA, 950 A9, Microchem)
- Copper etchant (CE-100, Transene)
- Poly(3,4-ethylenedioxythiophene)-block-poly(ethylene glycol) doped with perchlorate in nitromethane (PEDOT:PEG(PC), Sigma-Aldrich)
- Sulfonated poly(thiophene-3-[2-(2-methoxyethoxy)-ethoxy]-2,5-diyl) in ethylene glycol monobutyl ether/water (3:2) (RG-1200, Plexcore)

Appendix B

Associated Contributions

B.1 Publications

1. J. Jean, S. Chang, P. R. Brown, J. J. Cheng, P. H. Rekemeyer, M. G. Bawendi, S. Gradečak, V. Bulović, "ZnO Nanowire Arrays for Enhanced Photocurrent in PbS Quantum Dot Solar Cells," *Advanced Materials*, Early View, Feb. 2013, DOI: 10.1002/adma.201204192.

2. H. Park, S. Chang, J. Jean, J. J. Cheng, P. T. Araujo, M. Wang, M. G. Bawendi, M. Dresselhaus, V. Bulović, J. Kong, S. Gradečak, "Graphene Cathode-Based ZnO Nanowire Hybrid Solar Cells," *Nano Letters*, vol. 13, pp. 233-9, Jan. 2013.

B.2 Conference Presentations

1. P. R. Brown, J. Jean, T. P. Osedach, D. D. Wanger, N. Zhao, R. R. Lunt, M. G. Bawendi, V. Bulović, "Engineering Energy Level Alignment in Lead Sulfide Quantum Dot Photovoltaics through Ligand Exchange," presented at the 2013 Materials Research Society Spring Meeting, San Francisco, CA, 2013.

2. J. Jean, S. Chang, P. R. Brown, J. J. Cheng, P. H. Rekemeyer, M. G. Bawendi, S. Gradečak, V. Bulović, "Solution-Grown ZnO Nanowire Arrays for Quantum Dot Photovoltaics," poster presented at the Gordon Research Conference: Nanomaterials for Applications in Energy Technology, Ventura, CA, 2013.

3. P. R. Brown, J. Jean, T. P. Osedach, D. D. Wanger, N. Zhao, R. R. Lunt, M. G. Bawendi, V. Bulović, "Engineering Interfacial Energetics and Recombination in PbS QD Photovoltaics Through Ligand Exchange," poster presented at the Gordon Research Conference: Nanomaterials for Applications in Energy Technology, Ventura, CA, 2013.

4. A. Maurano, J. Macko, J. Jean, P. R. Brown, V. Bulović, "Recombination Dynamics of Charge Carriers in Nanostructured Solar Cells," poster presented at the Gordon Research Conference: Nanomaterials for Applications in Energy Technology, Ventura, CA, 2013.

5. J. Jean, S. Chang, P. R. Brown, J. J. Cheng, P. H. Rekemeyer, M. G. Bawendi, S. Gradečak, V. Bulović, "Solution-Grown ZnO Nanowire Arrays for Quantum Dot Photovoltaics," poster presented at the MIT Microsystems Technology Laboratories Annual Research Conference, Cambridge, MA, 2013.

6. J. Jean, S. Chang, P. R. Brown, J. J. Cheng, P. H. Rekemeyer, M. G. Bawendi, S. Gradečak, V. Bulović, "ZnO Nanowire Arrays for Enhanced Photocurrent in Quantum Dot Photovoltaics," presented at the 2012 Materials Research Society Fall Meeting, Boston, MA, 2012.

7. H. Park, S. Chang, J. Jean, J. J. Cheng, M. G. Bawendi, M. G. Bawendi, V. Bulović, J. Kong, and S. Gradečak, "Graphene Cathode-based Inverted ZnO Nanowire Hybrid Solar Cells via Interface Engineering," presented at the 2012 Materials Research Society Fall Meeting, Boston, MA, 2012.

8. J. Jean, S. Chang, P. R. Brown, J. J. Cheng, P. H. Rekemeyer, M. G. Bawendi, S. Gradečak, and V. Bulović, "Solution-Processed ZnO Nanowire Arrays for Quantum Dot Photovoltaics," poster presented at the 2012 MIT Energy Night, Cambridge, MA, 2012. *Runner-up for Best Poster Presentation Award.*

9. J. Jean, S. Chang, P. R. Brown, J. J. Cheng, P. H. Rekemeyer, M. G. Bawendi, S. Gradečak, and V. Bulović, "Solution-Processed ZnO Nanowire Arrays for Quantum Dot Photovoltaics," poster presented at the 2012 MIT Energy Initiative Fall Energy Research Conference, Cambridge, MA, 2012. *Best Poster Award.*

10. P. R. Brown, J. Jean, T. P. Osedach, D. D. Wanger, N. Zhao, R. R. Lunt, M. G. Bawendi, V. Bulović, "Engineering Interfacial Energetics and Recombination in PbS QD Photovoltaics Through Ligand Exchange," poster presented at the 2012 International Conference on Quantum Dots (QD2012), Santa Fe, NM, 2012.

Bibliography

[1] International Renewable Energy Agency, "Renewable Energy Technologies: Cost Analysis Series - Solar Photovoltaics." 2012.

[2] J. Jean, S. Chang, P. R. Brown, J. J. Cheng, P. H. Rekemeyer, M. G. Bawendi, S. Gradečak, and V. Bulović, "ZnO nanowire arrays for enhanced photocurrent in PbS quantum dot solar cells," *Advanced Materials*, Feb. 2013.

[3] U.S. Energy Information Administration, "Monthly Energy Review: Electricity Net Generation - Total (All Sectors)," tech. rep., U.S. Energy Information Administration (EIA), 2013.

[4] J. J. Choi, W. N. Wenger, R. S. Hoffman, Y.-F. Lim, J. Luria, J. Jasieniak, J. A. Marohn, and T. Hanrath, "Solution-processed nanocrystal quantum dot tandem solar cells," *Advanced Materials*, vol. 23, pp. 3144–8, July 2011.

[5] X. Wang, G. I. Koleilat, J. Tang, H. Liu, I. J. Kramer, R. Debnath, L. Brzozowski, D. A. R. Barkhouse, L. Levina, S. Hoogland, and E. H. Sargent, "Tandem colloidal quantum dot solar cells employing a graded recombination layer," *Nature Photonics*, vol. 5, pp. 480–484, June 2011.

[6] M. A. Hines and G. D. Scholes, "Colloidal PbS nanocrystals with size-tunable near-infrared emission: observation of post-synthesis self-narrowing of the particle size distribution," *Advanced Materials*, vol. 15, pp. 1844–1849, Nov. 2003.

[7] Y. Yin and A. P. Alivisatos, "Colloidal nanocrystal synthesis and the organic-inorganic interface," *Nature*, vol. 437, pp. 664–670, Sept. 2005.

[8] J. Tang and E. H. Sargent, "Infrared colloidal quantum dots for photovoltaics: fundamentals and recent progress," *Advanced Materials*, vol. 23, pp. 12–29, Jan. 2011.

[9] C. Wadia, A. P. Alivisatos, and D. M. Kammen, "Materials availability expands the opportunity for large-scale photovoltaics deployment," *Environmental Science & Technology*, vol. 43, pp. 2072–2077, Mar. 2009.

[10] J. Chen, W. Lei, C. Li, Y. Zhang, Y. Cui, B. Wang, and W. Deng, "Flexible quantum dot sensitized solar cell by electrophoretic deposition of CdSe quantum dots on ZnO nanorods," *Physical Chemistry Chemical Physics*, vol. 13, pp. 13182–4, Aug. 2011.

[11] K. W. Johnston, A. G. Pattantyus-Abraham, J. P. Clifford, S. H. Myrskog, D. D. MacNeil, L. Levina, and E. H. Sargent, "Schottky-quantum dot photovoltaics for efficient infrared power conversion," *Applied Physics Letters*, vol. 92, p. 151115, Apr. 2008.

[12] A. H. Ip, S. M. Thon, S. Hoogland, O. Voznyy, D. Zhitomirsky, R. Debnath, L. Levina, L. R. Rollny, G. H. Carey, A. Fischer, K. W. Kemp, I. J. Kramer, Z. Ning, A. J. Labelle, K. W. Chou, A. Amassian, and E. H. Sargent, "Hybrid passivated colloidal quantum dot solids," *Nature Nanotechnology*, vol. 7, pp. 577–82, Sept. 2012.

[13] R. R. Lunt, T. P. Osedach, P. R. Brown, J. A. Rowehl, and V. Bulović, "Practical roadmap and limits to nanostructured photovoltaics," *Advanced Materials*, vol. 23, pp. 5712–27, Dec. 2011.

[14] J. Jasieniak, M. Califano, and S. E. Watkins, "Size-dependent valence and conduction band-edge energies of semiconductor nanocrystals," *ACS Nano*, vol. 5, pp. 5888–902, July 2011.

[15] J. Tang, X. Wang, L. Brzozowski, D. A. R. Barkhouse, R. Debnath, L. Levina, and E. H. Sargent, "Schottky quantum dot solar cells stable in air under solar illumination," *Advanced Materials*, vol. 22, pp. 1398–402, Mar. 2010.

[16] R. Debnath, J. Tang, D. A. Barkhouse, X. Wang, A. G. Pattantyus-Abraham, L. Brzozowski, L. Levina, and E. H. Sargent, "Ambient-processed colloidal quantum dot solar cells via individual pre-encapsulation of nanoparticles," *Journal of the American Chemical Society*, vol. 132, pp. 5952–3, May 2010.

[17] J. M. Luther, J. Gao, M. T. Lloyd, O. E. Semonin, M. C. Beard, and A. J. Nozik, "Stability assessment on a 3% bilayer PbS/ZnO quantum dot heterojunction solar cell," *Advanced Materials*, vol. 22, pp. 3704–7, Sept. 2010.

[18] J. Gao, C. L. Perkins, J. M. Luther, M. C. Hanna, H.-Y. Chen, O. E. Semonin, A. J. Nozik, R. J. Ellingson, and M. C. Beard, "n-Type transition metal oxide as a hole extraction layer in PbS quantum dot solar cells," *Nano Letters*, vol. 11, pp. 3263–6, Aug. 2011.

[19] W. Ma, S. L. Swisher, T. Ewers, J. Engel, V. E. Ferry, H. A. Atwater, and A. P. Alivisatos, "Photovoltaic performance of ultrasmall PbSe quantum dots," *ACS Nano*, vol. 5, pp. 8140–7, Oct. 2011.

[20] J. M. Luther, M. Law, M. C. Beard, Q. Song, M. O. Reese, R. J. Ellingson, and A. J. Nozik, "Schottky solar cells based on colloidal nanocrystal films," *Nano Letters*, vol. 8, pp. 3488–92, Oct. 2008.

[21] A. K. Rath, M. Bernechea, L. Martinez, F. P. G. de Arquer, J. Osmond, and G. Konstantatos, "Solution-processed inorganic bulk nano-heterojunctions and their application to solar cells," *Nature Photonics*, vol. 6, pp. 529–534, July 2012.

[22] J. Tang, H. Liu, D. Zhitomirsky, S. Hoogland, X. Wang, M. Furukawa, L. Levina, and E. H. Sargent, "Quantum junction solar cells," *Nano Letters*, vol. 12, pp. 4889–94, Sept. 2012.

[23] K. W. Johnston, A. G. Pattantyus-Abraham, J. P. Clifford, S. H. Myrskog, S. Hoogland, H. Shukla, E. J. D. Klem, L. Levina, and E. H. Sargent, "Efficient Schottky-quantum-dot photovoltaics: The roles of depletion, drift, and diffusion," *Applied Physics Letters*, vol. 92, p. 122111, Mar. 2008.

[24] H. A. Atwater and A. Polman, "Plasmonics for improved photovoltaic devices," *Nature Materials*, vol. 9, pp. 205–13, Mar. 2010.

[25] J. M. Luther, M. Law, Q. Song, C. L. Perkins, M. C. Beard, and A. J. Nozik, "Structural, optical, and electrical properties of self-assembled films of PbSe nanocrystals treated with 1,2-ethanedithiol," *ACS Nano*, vol. 2, pp. 271–80, Feb. 2008.

[26] G. I. Koleilat, L. Levina, H. Shukla, S. H. Myrskog, S. Hinds, A. G. Pattantyus-Abraham, and E. H. Sargent, "Efficient, stable infrared photovoltaics based on solution-cast colloidal quantum dots," *ACS Nano*, vol. 2, pp. 833–40, May 2008.

[27] D. V. Talapin and C. B. Murray, "PbSe nanocrystal solids for n- and p-channel thin film field-effect transistors," *Science*, vol. 310, pp. 86–9, Oct. 2005.

[28] M. V. Kovalenko, M. Scheele, and D. V. Talapin, "Colloidal nanocrystals with molecular metal chalcogenide surface ligands," *Science*, vol. 324, pp. 1417–20, June 2009.

[29] J. Tang, K. W. Kemp, S. Hoogland, K. S. Jeong, H. Liu, L. Levina, M. Furukawa, X. Wang, R. Debnath, D. Cha, K. W. Chou, A. Fischer, A. Amassian, J. B. Asbury, and E. H. Sargent, "Colloidal-quantum-dot photovoltaics using atomic-ligand passivation," *Nature Materials*, vol. 10, pp. 765–71, Oct. 2011.

[30] P. Peumans, S. Uchida, and S. R. Forrest, "Efficient bulk heterojunction photovoltaic cells using small-molecular-weight organic thin films," *Nature*, vol. 425, pp. 158–62, Sept. 2003.

[31] G. Yu, J. Gao, J. C. Hummelen, F. Wudl, and A. J. Heeger, "Polymer photovoltaic cells: enhanced efficiencies via a network of internal donor-acceptor heterojunctions," *Science*, vol. 270, pp. 1789–1791, Dec. 1995.

[32] D. A. R. Barkhouse, R. Debnath, I. J. Kramer, D. Zhitomirsky, A. G. Pattantyus-Abraham, L. Levina, L. Etgar, M. Grätzel, and E. H. Sargent, "Depleted bulk heterojunction colloidal quantum dot photovoltaics," *Advanced Materials*, vol. 23, pp. 3134–8, July 2011.

[33] A. Kongkanand, K. Tvrdy, K. Takechi, M. Kuno, and P. V. Kamat, "Quantum dot solar cells. Tuning photoresponse through size and shape control of CdSe-TiO_2 architecture," *Journal of the American Chemical Society*, vol. 130, pp. 4007–15, Mar. 2008.

[34] K. S. Leschkies, R. Divakar, J. Basu, E. Enache-Pommer, J. E. Boercker, C. B. Carter, U. R. Kortshagen, D. J. Norris, and E. S. Aydil, "Photosensitization of ZnO nanowires with CdSe quantum dots for photovoltaic devices," *Nano Letters*, vol. 7, pp. 1793–8, June 2007.

[35] C. Luan, A. Vaneski, A. S. Susha, X. Xu, H.-E. Wang, X. Chen, J. Xu, W. Zhang, C.-S. Lee, A. L. Rogach, and J. A. Zapien, "Facile solution growth of vertically aligned ZnO nanorods sensitized with aqueous CdS and CdSe quantum dots for photovoltaic applications," *Nanoscale Research Letters*, vol. 6, p. 340, Jan. 2011.

[36] K. S. Leschkies, A. G. Jacobs, D. J. Norris, and E. S. Aydil, "Nanowire-quantum-dot solar cells and the influence of nanowire length on the charge collection efficiency," *Applied Physics Letters*, vol. 95, p. 193103, Nov. 2009.

[37] I. J. Kramer, D. Zhitomirsky, J. D. Bass, P. M. Rice, T. Topuria, L. Krupp, S. M. Thon, A. H. Ip, R. Debnath, H.-C. Kim, and E. H. Sargent, "Ordered nanopillar structured electrodes for depleted bulk heterojunction colloidal quantum dot solar cells," *Advanced Materials*, vol. 24, pp. 2315–9, May 2012.

[38] X. Lan, J. Bai, S. Masala, S. M. Thon, Y. Ren, I. J. Kramer, S. Hoogland, A. Simchi, G. I. Koleilat, D. Paz-Soldan, Z. Ning, A. J. Labelle, J. Y. Kim, G. Jabbour, and E. H. Sargent, "Self-assembled, nanowire network electrodes for depleted bulk heterojunction solar cells," *Advanced Materials*, vol. 25, pp. 1769–73, Mar. 2013.

[39] H. J. Fan, W. Lee, R. Hauschild, M. Alexe, G. Le Rhun, R. Scholz, A. Dadgar, K. Nielsch, H. Kalt, A. Krost, M. Zacharias, and U. Gösele, "Template-assisted large-scale ordered arrays of ZnO pillars for optical and piezoelectric applications," *Small*, vol. 2, pp. 561–8, Apr. 2006.

[40] C. Battaglia, J. Escarré, K. Söderström, M. Charrière, M. Despeisse, F.-j. Haug, and C. Ballif, "Nanomoulding of transparent zinc oxide electrodes for efficient light trapping in solar cells," *Nature Photonics*, vol. 5, pp. 535–538, Aug. 2011.

[41] L. Vayssieres, "Growth of arrayed nanorods and nanowires of ZnO from aqueous solutions," *Advanced Materials*, vol. 15, pp. 464–466, Mar. 2003.

[42] Z. L. Wang, "Zinc oxide nanostructures: growth, properties and applications," *Journal of Physics: Condensed Matter*, vol. 16, pp. R829–R858, June 2004.

[43] S. Xu and Z. L. Wang, "One-dimensional ZnO nanostructures: Solution growth and functional properties," *Nano Research*, vol. 4, pp. 1013–1098, Aug. 2011.

[44] L. E. Greene, M. Law, J. Goldberger, F. Kim, J. C. Johnson, Y. Zhang, R. J. Saykally, and P. Yang, "Low-temperature wafer-scale production of ZnO nanowire arrays," *Angewandte Chemie (International Ed. in English)*, vol. 42, pp. 3031–4, July 2003.

[45] H. Park, S. Chang, J. Jean, J. J. Cheng, P. T. Araujo, M. Wang, M. G. Bawendi, M. S. Dresselhaus, V. Bulović, J. Kong, and S. Gradečak, "Graphene cathode-based ZnO nanowire hybrid solar cells," *Nano Letters*, vol. 13, pp. 233–9, Jan. 2013.

[46] P. R. Brown, R. R. Lunt, N. Zhao, T. P. Osedach, D. D. Wanger, L.-Y. Chang, M. G. Bawendi, and V. Bulović, "Improved current extraction from ZnO/PbS quantum dot heterojunction photovoltaics using a MoO_3 interfacial layer," *Nano Letters*, vol. 11, pp. 2955–61, July 2011.

[47] O. E. Semonin, J. M. Luther, S. Choi, H.-Y. Chen, J. Gao, A. J. Nozik, and M. C. Beard, "Peak external photocurrent quantum efficiency exceeding 100% via MEG in a quantum dot solar cell," *Science*, vol. 334, pp. 1530–3, Dec. 2011.

[48] J. J. Choi, Y.-F. Lim, M. B. Santiago-Berrios, M. Oh, B.-R. Hyun, L. Sun, A. C. Bartnik, A. Goedhart, G. G. Malliaras, H. D. Abruña, F. W. Wise, and T. Hanrath, "PbSe nanocrystal excitonic solar cells," *Nano Letters*, vol. 9, pp. 3749–55, Nov. 2009.

[49] K. S. Leschkies, T. J. Beatty, M. S. Kang, D. J. Norris, and E. S. Aydil, "Solar cells based on junctions between colloidal PbSe nanocrystals and thin ZnO films," *ACS Nano*, vol. 3, pp. 3638–48, Nov. 2009.

[50] L. E. Greene, M. Law, D. H. Tan, M. Montano, J. Goldberger, G. Somorjai, and P. Yang, "General route to vertical ZnO nanowire arrays using textured ZnO seeds," *Nano Letters*, vol. 5, pp. 1231–1236, July 2005.

[51] P. Ruankham, L. Macaraig, T. Sagawa, H. Nakazumi, and S. Yoshikawa, "Surface modification of ZnO nanorods with small organic molecular dyes for polymer–inorganic hybrid solar cells," *The Journal of Physical Chemistry C*, vol. 115, pp. 23809–23816, Dec. 2011.

[52] M. Liu, A. Kitai, and P. Mascher, "Point defects and luminescence centres in zinc oxide and zinc oxide doped with manganese," *Journal of Luminescence*, vol. 54, pp. 35–42, Aug. 1992.

[53] X. Wang, G. I. Koleilat, A. Fischer, J. Tang, R. Debnath, L. Levina, and E. H. Sargent, "Enhanced open-circuit voltage in visible quantum dot photovoltaics by engineering of carrier-collecting electrodes," *ACS Applied Materials & Interfaces*, vol. 3, pp. 3792–5, Oct. 2011.

[54] H. Kim, C. M. Gilmore, A. Piqué, J. S. Horwitz, H. Mattoussi, H. Murata, Z. H. Kafafi, and D. B. Chrisey, "Electrical, optical, and structural properties of indium–tin–oxide thin films for organic light-emitting devices," *Journal of Applied Physics*, vol. 86, p. 6451, Dec. 1999.

[55] U.S. Geological Survey, "Mineral Commodity Summaries 2013," tech. rep., U.S. Geological Survey (USGS), 2013.

[56] Y. Leterrier, L. Médico, F. Demarco, J.-A. Månson, U. Betz, M. Escolà, M. Kharrazi Olsson, and F. Atamny, "Mechanical integrity of transparent conductive oxide films for flexible polymer-based displays," *Thin Solid Films*, vol. 460, pp. 156–166, July 2004.

[57] K. S. Novoselov, A. K. Geim, S. V. Morozov, D. Jiang, Y. Zhang, S. V. Dubonos, I. V. Grigorieva, and A. A. Firsov, "Electric field effect in atomically thin carbon films," *Science*, vol. 306, pp. 666–9, Oct. 2004.

[58] K. S. Novoselov, A. K. Geim, S. V. Morozov, D. Jiang, M. I. Katsnelson, I. V. Grigorieva, S. V. Dubonos, and A. A. Firsov, "Two-dimensional gas of massless Dirac fermions in graphene," *Nature*, vol. 438, pp. 197–200, Nov. 2005.

[59] K. S. Novoselov, D. Jiang, F. Schedin, T. J. Booth, V. V. Khotkevich, S. V. Morozov, and A. K. Geim, "Two-dimensional atomic crystals," *Proceedings of the National Academy of Sciences of the United States of America*, vol. 102, pp. 10451–3, July 2005.

[60] A. K. Geim, "Graphene: status and prospects," *Science*, vol. 324, pp. 1530–4, June 2009.

[61] Y.-J. Kim, J.-H. Lee, and G.-C. Yi, "Vertically aligned ZnO nanostructures grown on graphene layers," *Applied Physics Letters*, vol. 95, p. 213101, Nov. 2009.

[62] W. M. Choi, K.-S. Shin, H. S. Lee, D. Choi, K. Kim, H.-J. Shin, S.-M. Yoon, J.-Y. Choi, and S.-W. Kim, "Selective growth of ZnO nanorods on SiO_2/Si substrates using a graphene buffer layer," *Nano Research*, vol. 4, pp. 440–447, Feb. 2011.

[63] X. Li, W. Cai, J. An, S. Kim, J. Nah, D. Yang, R. Piner, A. Velamakanni, I. Jung, E. Tutuc, S. K. Banerjee, L. Colombo, and R. S. Ruoff, "Large-area synthesis of high-quality and uniform graphene films on copper foils," *Science*, vol. 324, pp. 1312–4, June 2009.

[64] A. Reina, X. Jia, J. Ho, D. Nezich, H. Son, V. Bulović, M. S. Dresselhaus, and J. Kong, "Large area, few-layer graphene films on arbitrary substrates by chemical vapor deposition," *Nano Letters*, vol. 9, pp. 30–5, Jan. 2009.

[65] S. Bae, H. Kim, Y. Lee, X. Xu, J.-S. Park, Y. Zheng, J. Balakrishnan, T. Lei, H. R. Kim, Y. I. Song, Y.-J. Kim, K. S. Kim, B. Ozyilmaz, J.-H. Ahn, B. H. Hong, and S. Iijima, "Roll-to-roll production of 30-inch graphene films for transparent electrodes," *Nature Nanotechnology*, vol. 5, pp. 574–8, Aug. 2010.

[66] S. Wang, Y. Zhang, N. Abidi, and L. Cabrales, "Wettability and surface free energy of graphene films," *Langmuir*, vol. 25, pp. 11078–81, Sept. 2009.

[67] H. Park, P. R. Brown, V. Bulović, and J. Kong, "Graphene as transparent conducting electrodes in organic photovoltaics: studies in graphene morphology, hole transporting layers, and counter electrodes," *Nano Letters*, vol. 12, pp. 133–40, Jan. 2012.

[68] M. M. de Kok, M. Buechel, S. I. E. Vulto, P. van de Weijer, E. A. Meulenkamp, S. H. P. M. de Winter, A. J. G. Mank, H. J. M. Vorstenbosch, C. H. L. Weijtens, and V. van Elsbergen, "Modification of PEDOT:PSS as hole injection layer in polymer LEDs," *physica status solidi (a)*, vol. 201, pp. 1342–1359, May 2004.

[69] W. W. Chiu, J. Travaš-Sejdić, R. P. Cooney, and G. A. Bowmaker, "Studies of dopant effects in poly(3,4-ethylenedioxythiophene) using Raman spectroscopy," *Journal of Raman Spectroscopy*, vol. 37, pp. 1354–1361, Dec. 2006.

[70] S. Sakamoto, M. Okumura, Z. Zhao, and Y. Furukawa, "Raman spectral changes of PEDOT–PSS in polymer light-emitting diodes upon operation," *Chemical Physics Letters*, vol. 412, pp. 395–398, Sept. 2005.